Biomimetic biphasic curdlan-based scaffold for osteochondral tissue engineering applications – Characterization and preliminary evaluation of mesenchymal stem cell response *in vitro*

Katarzyna Klimek[a,*], Aleksandra Benko[b], Marta Vandrovcova[c], Martina Travnickova[c], Timothy E.L. Douglas[d,e], Marta Tarczynska[f], Antonin Broz[c], Krzysztof Gaweda[f], Grazyna Ginalska[a], Lucie Bacakova[c]

[a]Medical University of Lublin, Chair and Department of Biochemistry and Biotechnology, Chodzki 1 Street, 20-093 Lublin, Poland

[b]AGH University of Science and Technology, Faculty of Materials Science and Ceramics, 30 A. Mickiewicza Av., 30-059 Krakow, Poland

[c]Institute of Physiology of the Czech Academy of Sciences, Laboratory of Biomaterials and Tissue Engineering, Videnska 1083 Street, 14220 Prague, Czech Republic

[d]Engineering Department, Lancaster University, Gillow Avenue, LA1 4YW Lancaster, United Kingdom

[e]Materials Science Institute (MSI), Lancaster University, Lancaster, United Kingdom

[f]Medical University of Lublin, Department and Clinic of Orthopaedics and Traumatology, Jaczewskiego 8 Street, 20-090 Lublin, Poland

Corresponding author:

*Dr. Katarzyna Klimek; E-mail: katarzyna.klimek@umlub.pl

Abstract

Osteochondral defects remain a huge problem in medicine today. Biomimetic bi- or multi-phasic scaffolds constitute a very promising alternative to osteochondral autografts and allografts. In this study, a new curdlan-based scaffold was designed for osteochondral tissue engineering applications. To achieve biomimetic properties, it was enriched with a protein component – whey protein isolate as well as a ceramic ingredient – hydroxyapatite granules. The scaffold was fabricated via a simple and cost-efficient method, which represents a significant advantage. Importantly, this technique allowed generation of a scaffold with two distinct, but integrated phases. Scanning electron microcopy and optical profilometry observations demonstrated that phases of biomaterial possessed different structural properties. The top layer of the biomaterial (mimicking the cartilage) was smoother than the bottom one (mimicking the subchondral bone), which is beneficial from a biological point of view because unlike bone, cartilage is a smooth tissue. Moreover, mechanical testing showed that the top layer of the biomaterial had mechanical properties close to those of natural cartilage. Although the mechanical properties of the bottom layer of scaffold were lower than those of the subchondral bone, it was still higher than in many analogous systems. Most importantly, cell culture experiments indicated that the biomaterial possessed high cytocompatibility towards adipose tissue-derived mesenchymal stem cells and bone marrow-derived mesenchymal stem cells *in vitro*. Both phases of the scaffold enhanced cell adhesion, proliferation, and chondrogenic differentiation of stem cells (revealing its chondroinductive properties *in vitro*) as well as osteogenic differentiation of these cells (revealing its osteoinductive properties *in vitro*). Given all features of the novel curdlan-based scaffold, it is worth noting that it may be considered as promising candidate for osteochondral tissue engineering applications.

Key words: β-1,3-glucan, biphasic scaffold, osteochondral defects, regenerative medicine, stem cells, tissue engineering

Abbreviations: 3D, three-dimensional; ACI, autologous chondrocyte implantation; ADSCs, adipose tissue-derived mesenchymal stem cells; ATR-FTIR, attenuated total reflectance Fourier-transform infrared spectroscopy; BMDSCs, bone marrow-derived mesenchymal stem cells; BSA, bovine serum albumin; DMEM, Dulbecco's Modified Eagle Medium; E, Young's modulus; FBS, fetal bovine serum; FEG-SEM, field emission gun scanning electron microscope; FTIR, Fourier transform infrared spectroscopy; GAGs, glycosaminoglycans; HAp, hydroxyapatite; hFGF-2 – recombinant human fibroblast growth factor-basic; MSCs, mesenchymal stem cells; OA, osteoarthritis; PBS, phosphate-buffered saline; R_a, arithmetic average height; R_p, maximum height of peaks; R_q, root mean square roughness; R_t, maximum height of the profile; R_v, maximum depth of valleys; SD, standard deviation; TEP, tissue engineering products; WPI, whey protein isolate;

1. Introduction

Osteochondral defects most often result from severe traumas, athletic injuries, as well as diseases. A possible accompanying complication is osteoarthritis (OA), which results in degradation of cartilage and the underlying subchondral bone, representing a very serious ailment for orthopedic patients [1]. Because the cartilage and subchondral bone have different biological, structural, and mechanical properties, the treatment of osteochondral lesions still constitutes an arduous challenge for clinicians. Currently, traditional therapies involve arthroscopic debridement, abrasion arthroplasty/chondroplasty, microfracture, and autologous chondrocyte implantation (ACI). Nevertheless, these treatments usually do not allow for complete and simultaneous regeneration of the cartilage and the subchondral bone [2–5]. Another treatment, namely mosaicplasty, involving the use of autografts or allografts, provides better therapeutic effects, but it also possesses some disadvantages, such as limited availability, secondary traumatization connected with additional pain (in the case of autografts) or to the risk of inducing an unfavorable immune response (in the case of allografts) [6–8].

To overcome limitations associated with traditional treatment methods, tissue engineering products (TEP) are increasingly being used [1,9–13]. This approach includes application of scaffolds, which have the ability to mimic natural tissues, typically combined with cell of different origins (exogenous or endogenous). To date, various mono-, bi-, and multi-phasic bioactive scaffolds have been developed for osteochondral defect regeneration. Taking into consideration the complex structure of the osteochondral tissue, the bi- and multi-phasic scaffolds have more favorable properties compared to monophasic biomaterials [2,9,12,14–16]. Numerous studies have proven that the bi- and multi-phasic scaffolds had the ability to support the adhesion, proliferation, and differentiation of mesenchymal stem cells (MSCs) *in vitro,* both chondrogenic and osteogenic [17–20]. Moreover, they have been found to induce the regeneration of both cartilage and subchondral bone *in vivo* [12,14,19,21]. Some clinical results also demonstrated the safety and therapeutic efficacy of bi- and multi-phasic osteochondral scaffolds [2,22].

The aim of this study was to develop a novel, biomimetic, and biphasic curdlan-based biomaterial for osteochondral tissue engineering applications. Curdlan is a natural β-glucan synthesized by the *Agrobacterium species* [23,24]. This polysaccharide has been successfully applied in the food industry, pharmacy, and medicine, in particular due to its cytocompatibility and its ability to form an elastic gel. It was demonstrated that curdlan may form different types of gels, depending on the applied conditions [24–26]. Importantly, a curdlan gel whose formation is induced by heating to above 90°C, produced from its aqueous suspension, was found to be an appropriate ingredient of the polymer-bioceramic biomaterials for bone tissue engineering applications. The resultant bone scaffolds were characterized by good surgical handling, bioactivity, and biocompatibility, both *in vitro* and *in vivo* [27–29]. In this study, we attempted to use the thermally-obtained curdlan gel (temp. > 90°C) as a main component of a scaffold with the aim of mimicking natural osteochondral tissue. In order to provide biomimetic and biphasic properties, the scaffold was enriched with a protein component – whey protein isolate (WPI), and with a bioceramic constituent – hydroxyapatite (HAp) granules. The choice of WPI was motivated by its favorable biological features, with several studies demonstrating an excellent performance when incorporated into bioceramic-based bone scaffolds [30–32]. It was found that such scaffolds supported osteoblast adhesion, proliferation, and differentiation [30–32]. Combining a reducing polysaccharide with a mixture of proteins (such as WPI) is expected to produce biomaterials with enhanced mechanical properties (thanks to Maillard reaction [33]) and improved biological performance as proteins possess cell-recognizable motifs, which are not present in other biopolymers [34]. Additionally, the usage of WPI is cost-efficient (as compared to other proteins), and the material is characterized by good physicochemical properties, and the ability to create a firm, thermally-formed gel (temp. > 90°C – the same as that used for fabrication of thermally-obtained curdlan gel) [30,35,36]. In turn, synthetic HAp granules were added to the biomaterial in order to mimic a natural mineral ingredient of bone [25,37]. The proposed scaffold was fabricated using an uncomplicated, fast, and cost-efficient technique. The simplicity of the process constitutes its indisputable advantage over alternative methods applied for fabrication of other biphasic biomaterials, which are often more complex and expensive [16,19,20]. It is assumed that novel curdlan-based biomaterial could be a promising scaffold for osteochondral tissue engineering applications, thanks to its composition, structure, mechanical, and biological properties as well as the ease and cost-efficiency of the fabrication method. We suppose that the obtained biomaterial can mimic biochemical and mechanical properties of the cartilage tissue as well as subchondral bone tissue, and as a consequence can promote chondrogenic and osteogenic differentiation of stem cells.

In order to confirm the hypothesis, the biomaterial was subjected to a thorough analyses. The macro/microstructure and the topography of the newly developed biomaterial were characterized by stereoscopic microscopy, scanning electron microscopy (SEM), and optical profilometry. A compression test was performed in order to assess the material's Young's modulus. The potential physicochemical interactions between curdlan, WPI, and HAp in the biomaterial were assessed using Fourier transform infrared spectroscopy (FTIR). Moreover, comprehensive cell culture experiments using adipose tissue-derived mesenchymal stem cells (ADSCs) and bone marrow-derived mesenchymal stem cells (BMDSCs) were conducted to evaluate the biomaterial's ability to support the cell adhesion, proliferation, and induction of chondrogenic and osteogenic differentiation. It is worth underlining that, due to the innovative features of the aforementioned curdlan-based biomaterial, its fabrication method, composition, and properties were described in the Polish patent application no. P.437234 entitled "Biphasic biomaterial based on curdlan and hydroxyapatite (HAp) for regeneration of osteochondral defects and the method of its preparation". According to the best of our knowledge, this is the first study in which a biphasic curdlan-based biomaterial for osteochondral tissue engineering applications was fabricated and characterized. The innovation of the proposed curdlan-based biomaterial, compared to other biomaterials composed of this polysaccharide, lies in its composition, structure, and potential biomedical application [25,29,38–43]. Thanks to mixing curdlan with WPI, new, unparalleled properties are expected of the biomaterial.

2. Materials and methods

2.1. Fabrication of curdlan-based osteochondral scaffold

Firstly, HAp granules were prepared as reported previously [25]. Then, 0.08 g curdlan powder (80 kDa, WAKO pure Chemicals Industries, Japan) was placed in an eppendorf tube (volume 2 mL) and then 1 ml of a water solution of 30 wt.% WPI (BiPRO, Davisco Foods

International, Agropur Cooperative, USA) was added. Subsequently, 0.7 g of HAp granules (0.05-0.2 mm in diameter) was gradually suspended in curdlan/WPI solution. The mixture was centrifuged (3 min., 3000 rpm; Centrifuge MiniSpin® plus, Eppendorf, Poland) to obtain two visible phases and finally it was heated at 90°C for 15 minutes (Fixed Dry Block Heater, BTD, Grant Instruments, USA). Afterwards, the sample was removed from the centrifuge tube and dried in air for 24 hours. For further analyses (structure/topography characterization, FTIR measurements, mechanical tests, ion release tests, and cell culture experiments), the biomaterials composed only of curdlan, WPI, curdlan/WPI or curdlan/WPI/HAp were prepared according to the same procedure. All samples were sterilized by ethylene oxide (55°C, 3 hours). The fabricated biomaterials are summarized in Table 1.

Table 1. Composition, type, size, and shape of fabricated curdlan-based biomaterials.

Biomaterial type and composition	Biomaterial code	Biomaterial shape and size	Analysis
Curdlan-based biomaterial (8 wt.% of curdlan)	Cur	Cylinder shape, approx. 3 mm in height	FTIR measurements
WPI -based biomaterial (30 wt.% of WPI)	WPI	Cylinder shape, approx. 3 mm in height	FTIR measurements
Biomaterial mimicking “cartilage layer” (8 wt.% of curdlan and 30 wt.% of WPI)	Cur/WPI	Cylinder shape, approx. 3 mm in height	FTIR measurements, optical profilometry, ion reactivity test, cell culture experiments
		Cylinder shape, approx. 10 mm in height	Mechanical tests
Biomaterial mimicking “subchondral bone layer” (8 wt.% of curdlan, 30 wt.% of WPI, 0.7 g of HAp granules	Cur/WPI/HAp	Cylinder shape, approx. 3 mm in height	FTIR measurements, optical profilometry, ion reactivity test, cell culture experiments
		Cylinder shape, approx. 10 mm in height	Mechanical tests
Biphasic scaffold mimicking “osteochondral tissue” (8 wt.% of curdlan, 30 wt.%	Cur/WPI – Cur/WPI/HAp	Cylinder shape, approx. 10 mm in height	Stereoscopic microscopy, scanning electron microscopy, mechanical tests, swelling ability

of WPI, 0.7 g of HAp granules)			

2.2. Characterization of macro/microstructure and topography

The macrostructure of biphasic curdlan-based scaffold was evaluated using a stereoscopic microscope (Olympus SZ61TR, Olympus, Poland). An exemplary sample harvested during standard mosaicplasty was used for comparison. The surgical procedure was performed in accordance with the guidelines of the Declaration of Helsinki, and this study was approved by the Bioethics Committee of Medical University of Lublin, Poland (approval no. KE-0254/114/2020 from June 2020). The patient gave his written informed consent for his biological material to be used for research purposes.

In turn, the microstructure of biomaterial cross-section was characterized by a field emission gun scanning electron microscope (FEG-SEM, JSM-7800F, Joel Ltd., Japan), using a lower secondary electron detector. Prior to analysis, the sample was mounted on standard aluminium pin stubs using double-sided conductive carbon adhesive dots. Then, its surface was coated with approx. 5 nm of gold (at 20 mA for 60 s, 1x 10^{-2} mBar, under argon) using a gold sputter coater (Q150RES, Quorum Technologies Ltd., UK).

The topography of the top and bottom layers of the scaffold was visualized by an optical profilometer (Contour GT-K1-3D Optical Profiler, Bruker, USA). During the measurement, the following parameters were applied: processing method – VXI, scan area – 583 µm x 437 µm, resolution – 0.911 µm (x,y positions), and 5 nm (z position). The three-dimensional (3D) images were obtained using Vision64 Map Software (Bruker, USA). Moreover, the characteristic parameters of the sample roughness [44], namely arithmetic average height (R_a), maximum height of peaks (R_p), root mean square roughness (R_q), maximum height of the profile (R_t), and maximum depth of valleys (R_v) were determined (Vision64 Map Software, Bruker, USA).

2.3. Fourier-transformed infrared spectroscopy

Attenuated total reflectance Fourier-transform spectroscopy (ATR-FTIR, Bruker Tensor 27, PIKE MIRacle diamond ATR accessory) was used for the identification of chemical composition and possible interactions between the composite's components. Prior to measurements, the samples were stored in a desiccator. The specimens were cut into small pieces and ground in a mortar to obtain a homogenous powder. An average of 128 scans with a spectral resolution of 4 cm^{-1} were recorded in the mid infrared region (4000 – 500 cm^{-1}). The OPUS 7.2 software was used for a manual baseline correction and smoothing (9 smoothing points). The as-obtained spectra were visualized using the OriginPro 2021 Software.

2.4. Evaluation of the Young's modulus

The compression tests were conducted using an INSTRON 3345 testing machine (Instron®, Norwood, MA, USA) with a 10 N load cell. Prior to experiments, the samples were equilibrated in 0.9% normal saline solution (NaCl, Sigma-Aldrich, USA), and the analyses were conducted in a wet state. Each sample was subjected to a preload of 1 N and then compressed at a basic load rate of 0.5 mm/min until the maximum load of 10N + preload was reached. Measurements, such as displacement (mm), force (N), and time, were obtained after each test, which was then used to calculate the compressive stress (σ), compressive strain (ε), and consequentially the biomaterial's Young's modulus (E). The experiment was carried out using 5 independent samples of biomaterials.

2.5. Evaluation of swelling ability

The experiment was carried out according to the procedure described in detail previously [25]. Briefly, three separate samples of biphasic Cur/WPI-Cur/WPI/HAp biomaterial were soaked in 0.9% NaCl solution. The biomaterials' ability to swell was determined as an increase in its weight (Wi) over time. The following equation was used for calculation of Wi:

$$Wi = \frac{(Wt - W0)}{W0} \times 100\%,$$

Where Wt denotes biomaterial weight at specified time of soaking, while W0 denotes biomaterial weight before the experiment.

2.6. Evaluation of ion release

To assess the changes in the profiles of Ca^{2+} and HPO_4^{2-} ions, the samples were placed in 500 µl of culture medium, i.e., Dulbecco's Modified Eagle Medium (DMEM, Gibco^{TM}, ThermoFisher Scientific, USA) and incubated for 15 days (37°C, 5% CO_2, Heraeus Cytoperm 2, ThermoFisher Scientific, USA). The medium was collected every third day and then a new portion was added (this procedure was applied in order to achieve equal conditions to those used during cell culture experiments *in vitro*). The concentration of ions was measured using Calcium CPC and Phosphorus ions detection kits (Biomaxima, Poland).

2.7. Evaluation of stem cell response

2.7.1. Cell models and culture conditions

Human adipose tissue-derived mesenchymal stem cells (ADSCs) were isolated from an adipose tissue obtained during liposuction, as described in detail previously [39,45]. The surgical procedure was performed in accordance with the guidelines of the Declaration of Helsinki, and this study was approved by the Ethics Committee of Hospital Na Bulovce in Prague (approval from June 11, 2019). The patient gave her written informed consent to the use of her biological material for research purposes. The ADSCs originated from a single donor (healthy woman, 46 years). These cells were isolated in the Institute of Physiology of the Czech Academy of Sciences, Laboratory of Biomaterials and Tissue Engineering (Prague, Czech Republic) from a lipoaspirate taken by liposuction from a thigh region in the Hospital Na Bulovce in Prague. In brief, the lipoaspirate was washed several times with PBS and subsequently enzymatically digested using collagenase type I (Worthington Biochemical Corp., USA). The lipoaspirate containing collagenase solution was then centrifuged and upper layers containing mature adipocytes and digested tissue were removed. The remaining lowest part containing ADSCs (i.e., stromal vascular fraction layer) was washed with DMEM (Gibco^{TM}, ThermoFisher Scientific, USA), filtered through a 100 μm strainer, and seeded into culture flasks. In passage 2, the cells were characterized by flow cytometry for the presence of the following markers typical for stem cells: CD105 (endoglin; 99.9% of positive cells), CD90 (immunoglobulin Thy-1; 99.5%), CD73 (ecto-5'-nucleotidase; 100%), CD29 (fibronectin receptor; 100%), and for negativity or low expression of markers of other cell types, such as pericytes (CD146- melanoma cell adhesion molecule, receptor for laminin; 4.7%), endothelial cells CD31 (platelet-endothelial cell adhesion molecule-1, PECAM-1; 0.5%), and hematopoietic cells, namely CD34 (an antigen of hematopoietic progenitor cells; 0.2%), and CD45 (protein tyrosine phosphatase receptor type C; 3.8%) (for a review, see [46,47]). The ADSCs were cultured in DMEM with the addition of 10% of fetal bovine serum (FBS, Gibco^{TM}, ThermoFisher Scientific, USA), 10 ng/ml of recombinant human fibroblast growth factor-basic (hFGF-2, GenScript, USA), and 40 μg/ml of gentamicin (Lek d.d., Slovenia). In turn, human bone marrow-derived mesenchymal stem cells (BMDSCs, Cat. No. 7500, https://www.sciencellonline.com/human-bone-marrow-derived-mesenchymal-stem-cells.html) were purchased from ScienCell Research Laboratories (USA). The BMDSCs were cultured in Mesenchymal Stem Cell Medium (MSCM, ScienCell Research Laboratories, USA) supplemented with 10% FBS, 1% Mesenchymal Stem Cell Growth Supplement (MSCGS, ScienCell Research Laboratories, USA), and 40 μg/ml gentamicin. Both types of stem cells were cultured in the humidified incubator providing 37°C and 5% CO_2 (Thermo Electron Corporation, USA) and can be classified as primary low-passaged cells (used in passages 1-3), i.e., not cell lines. Either ADSCc and BMDSCs were seeded onto scaffolds at passage 3.

2.7.2. Cell adhesion and spreading

The ADSCs and BMDSCs were detached from the culture flasks by trypsinization and suspended in their growth media described above. The number of cells was determined using a Vi-CELL XR Cell Viability Analyzer (Beckman Coulter, USA). Subsequently, 500 µl of cell suspension containing 50.000 cells was seeded directly on biomaterials (the initial number of cells was established from our earlier experiments). After 2-day incubation, the cells grown on the biomaterials were washed with phosphate-buffered saline (PBS, Sigma-Aldrich, USA), fixed for 15 min. with 4% paraformaldehyde (Sigma-Aldrich, USA) prepared in PBS, permeabilized first with 0.1% Triton X-100 (Sigma-Aldrich, USA) prepared in 1% bovine serum albumin solution (BSA, Sigma-Aldrich, USA), and then with 1% Tween 20 (Sigma-Aldrich, USA) prepared in PBS. Subsequently, the F-actin cytoskeleton was counterstained with phalloidin conjugated with TRITC (Sigma-Aldrich, USA) and the cell nuclei were counterstained with 0.5 µg/ml Hoechst 33342 (Sigma-Aldrich, USA). The cells were observed under an Andor Dragonfly 503 scanning disc confocal microscope equipped with a Zyla 4.2 PLUS sCMOS camera, objective HC PL APO 10x/0.40 DRY CS2 (Andor Technology Ltd., UK). Six independent images were taken for each sample. Total cell spreading area, i.e., the total area on the biomaterial surface occupied by all adhering cells, was measured using ImageJ 1.52v software (Wayne Rasband, USA) according to the protocol created by Baviskar [48]. Moreover, the cell nuclei were counted using blue-channel images (ImageJ 1.52v software,Wayne Rasband, USA). Then, average spreading area per cell was calculated using the following formula:

$$Average\ spreading\ area\ [\mu m^2\ per\ cell] = \frac{total\ spreading\ area\ [\mu m^2]}{total\ number\ of\ cells}$$

2.7.3. Cell proliferation

The ADSCs and BMDSCs were detached from culture flask and suspended in culture medium. The number of cells was determined using a Vi-CELL XR Cell Viability Analyzer

(Beckman Coulter, USA). Subsequently, 500 μl of cell suspension containing 25.000 cells was seeded directly on biomaterials and polystyrene – PS (control). This number of cells was established from our earlier experiments. Lower density of cells used for this experiment was chosen in order to avoid contact inhibition at the longer culture times on PS. After 2-, 5-, and 8-day incubation, cell proliferation was assessed by a resazurin test, according to the manufacturer's guidelines (Sigma-Aldrich, USA). This assay is based on the reduction of resazurin (non-fluorescent, blue dye) into resorufin (fluorescent, pink dye) by viable, metabolically active cells. The samples were measured fluorometrically (Ex = 530 nm; Em = 590 nm) using Synergy^{TM} HT Multi-Mode Microplate Reader (BioTek, USA).

2.7.4. Cell differentiation

The ADSCs and BMDSCs were detached from the culture flasks and suspended in their growth media. The number of cells was determined using a Vi-CELL XR Cell Viability Analyzer (Beckman Coulter, USA). Subsequently, 500 μl of cell suspension containing 50.000 cells was seeded directly on biomaterials (this number of cells was established from our earlier experiments). The cells were pre-cultured for 5 days in the growth culture media (details were described in Section 2.7.1), and afterwards, the media were replaced by the chondrogenic or osteogenic ones. These media were prepared by supplementation of the growth culture media with differentiation ingredients purchased from Sigma-Aldrich, USA (Table 2). The cells were cultured for another 10 days. Differentiation media were changed every two days. The selected culture time was based on our earlier experiments, where it has been proven that both ADSCs and BMDSCs are able to produce differentiation markers as early as on the 6th day of culture [39].

Table 2. List of supplements added to growth culture media in order to induce chondrogenic or osteogenic differentiation of ADSCs and BMDSCs.

Chondrogenic medium	Osteogenic medium

0.05 mg/ml ascorbic acid 10^{-7} M dexamethasone 10% ITS Liquid Media Supplement 10 ng/ml TGF-β1 10 ng/ml BMP-6	0.05 mg/ml ascorbic acid 10^{-8} M dexamethasone 10 mM β-glycerophosphate

Subsequently, the cells were fixed and permeabilized as described above (Section 2.7.2). For evaluation of typical chondrogenic markers, the cells were stained with a primary mouse anti-collagen type II monoclonal antibody (Sigma-Aldrich, USA) – diluted 1:200 in PBS, a primary mouse anti-aggrecan monoclonal antibody (Santa Cruz Biotechnology, USA) – diluted 1:50 in PBS, and a primary mouse anti-SOX-9 monoclonal antibody (Santa Cruz Biotechnology, USA) – diluted 1:50 in PBS. In turn, for assessment of typical osteogenic markers, the cells were stained with a primary rabbit polyclonal anti-collagen type I antibody (Cosmo Bio Co., Ltd., Japan) – diluted 1:200 in PBS, a primary mouse anti-alkaline phosphatase/ALPL monoclonal antibody (R&D Systems, Inc., USA) – diluted 1:200 in PBS, and a primary rabbit polyclonal anti-osteocalcin antibody (Peninsula Laboratories Inc., USA) – diluted 1:200 in PBS. Then, the cells were labeled with a secondary goat anti-mouse IgG (H+L) antibody conjugated with AlexaFluor® 488 (Invitrogen, ThermoFisher Scientific, USA) – diluted 1:400 in PBS or a secondary goat anti-rabbit IgG (H+L) antibody conjugated with AlexaFluor® 488 (Invitrogen, ThermoFisher Scientific, USA) – diluted 1:400 in PBS. The cell nuclei were counterstained with 0.5 μg/ml of Hoechst 33342 (Sigma-Aldrich, USA) added to the solutions with the secondary antibodies.

2.8. Statistical analysis

The experiments were carried out in at least three independent replicates. The obtained results were shown as mean values ± standard deviation (SD). To establish statistical differences between the investigated groups ($P < 0.05$), a One-Way ANOVA test, followed by a Tukey's multiple comparison test were applied (GraphPad Prism 5, Version 5.04 Software).

3. Results and discussion

3.1. Macro/microstructure and topography

An osteochondral tissue has a complex structure because it is composed of cartilage and the underlying subchondral bone. The cartilage mainly comprises water, glycosaminoglycans (GAGs), and type II collagen, while the subchondral bone's major compounds are water, hydroxyapatite (HAp), and type I collagen. According to the available literature, the most promising biomaterials designed for the osteochondral defect regeneration (i.e., bi- or multi-phasic scaffolds), should be composed of natural or synthetic polymers in the layer mimicking the "cartilage" and bioceramics or a polymer-bioceramics mixture in the layer mimicking the "subchondral bone". The use of such biomaterials allows creation of constructs with composition and properties similar to those of natural tissues [1,2,11,14,15,20,21,49]. The biphasic scaffold obtained in this study (Fig. 1A) was composed of a polymer-based phase (curdlan/WPI), mimicking the "cartilage layer" (approx. 2-3 mm in height) and of a polymer-ceramic phase (curdlan/WPI/HAp) mimicking the "subchondral bone layer" (approx. 7-8 mm in height). Thus, not only the composition of the fabricated biomaterial, but also its macrostructure was similar to that of an osteochondral autograft (Fig. 1B).

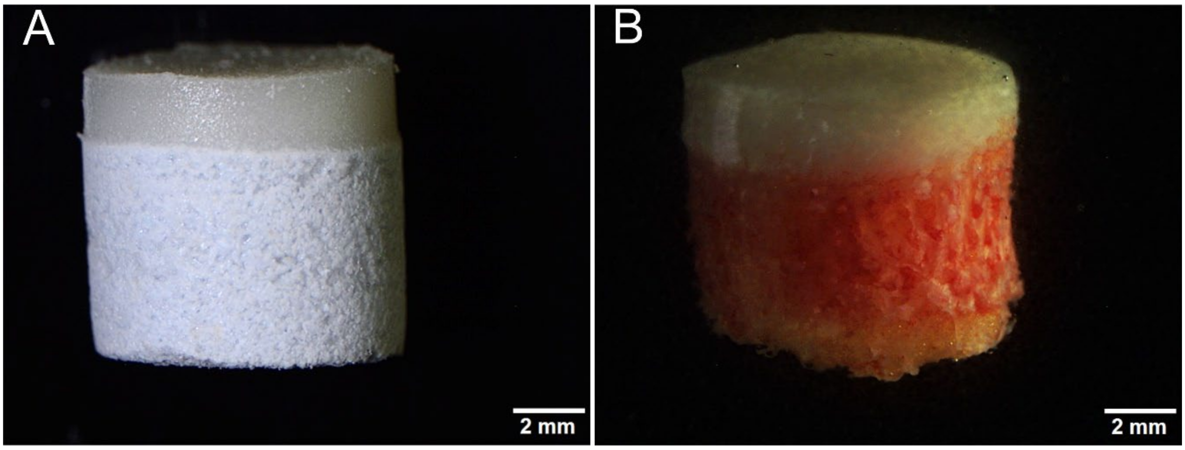

Fig. 1. Stereoscopic microscope images showing a biphasic curdlan-based osteochondral scaffold (A) and an example of osteochondral autograft harvested during mosaicplasty procedure (B); magnification 8x, scale bar = 2 mm.

It is worth underlining that even though the multiphasic scaffolds attract a great attention in the field of osteochondral tissue engineering, they also possess some drawbacks. Primarily, their fabrication process most often requires combination of independent layers before or during the implantation. In many cases, separation of the biomaterial's layers was observed after the surgery, which in consequence resulted in instability of the scaffold and the need for its removal. The development of stable scaffolds with no tendency to delaminate at the interface is therefore crucial in achieving promising biomaterials for osteochondral tissue engineering applications [11,13,37,50]. In this study, the applied fabrication procedure allowed production of a biphasic curdlan-based scaffold with a well-defined structure. The SEM images proved that this biomaterial contained two distinct, but integrated phases (Fig. 2A). The top layer of scaffold (mimicking the "cartilage layer"), composed of curdlan and WPI (Fig. 2B), possessed a visually smoother microstructure, as compared to the bottom layer of biomaterial (mimicking the "subchondral bone layer"), which comprised curdlan, WPI, and HAp granules (Fig. 2C).

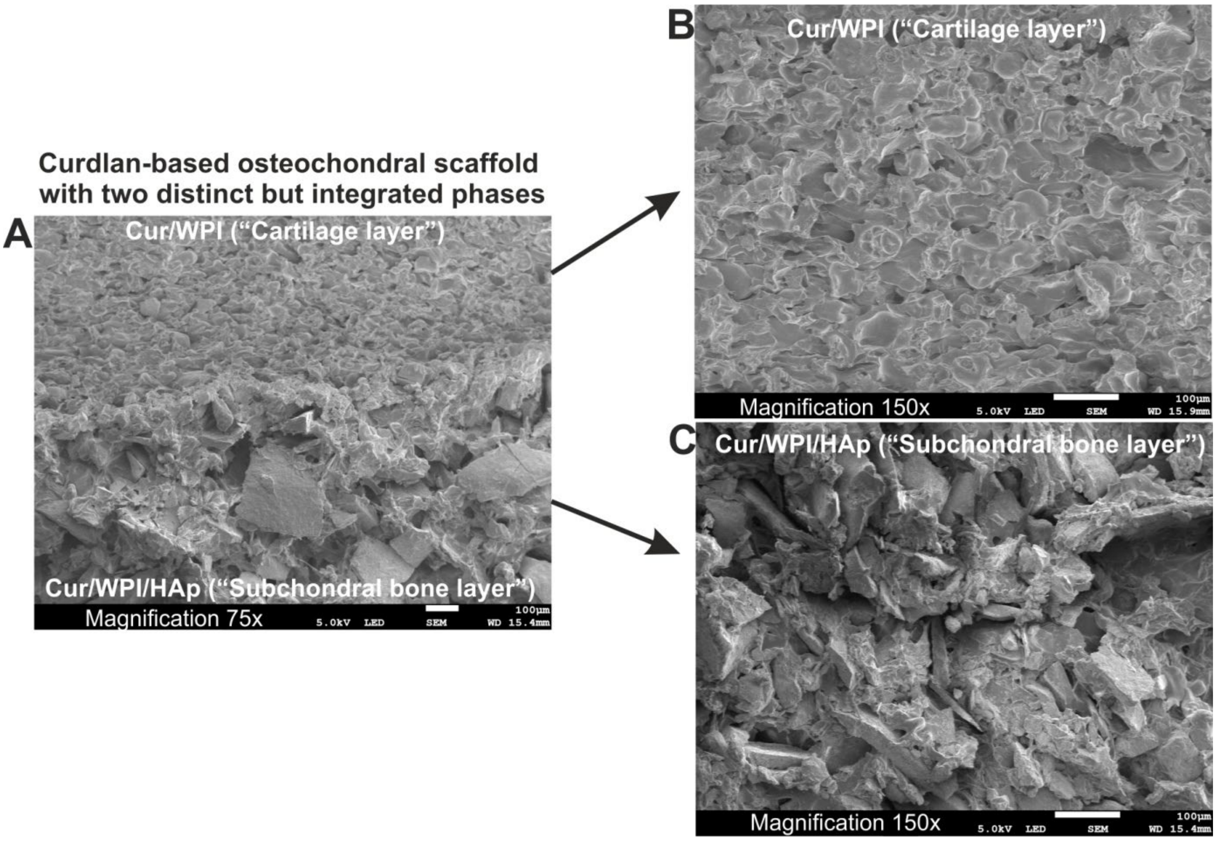

Fig. 2. Scanning electron microscope images showing longitudinal cross-section of a biphasic curdlan-based scaffold (A), the top layer (B) and the bottom layer (C) of this biomaterial; magnification 75x or150x, scale bar = 100 µm.

To assess the roughness of individual phases of the fabricated scaffold, the surface of top (Fig. 3A) and bottom (Fig. 3B) layers of biomaterial were visualized using optical profilometry. It was demonstrated that the surface of Cur/WPI/HAp, thanks to the presence of HAp granules, possessed a roughness approximately 3 times higher (considering R_a, R_p, R_q, R_t, and R_v values) than that of the Cur/WPI (Fig. 3C). It is worth noting that the surface roughness is a crucial feature of biomaterials, which affects the adhesion, proliferation, and differentiation of mesenchymal stem cells (MSCs) [51–54]. The influence of the surface roughness of our biphasic curdlan-based biomaterial on the stem cell behavior was assessed in a later part of this study (3.6. *In vitro* biocompatibility with stem cells).

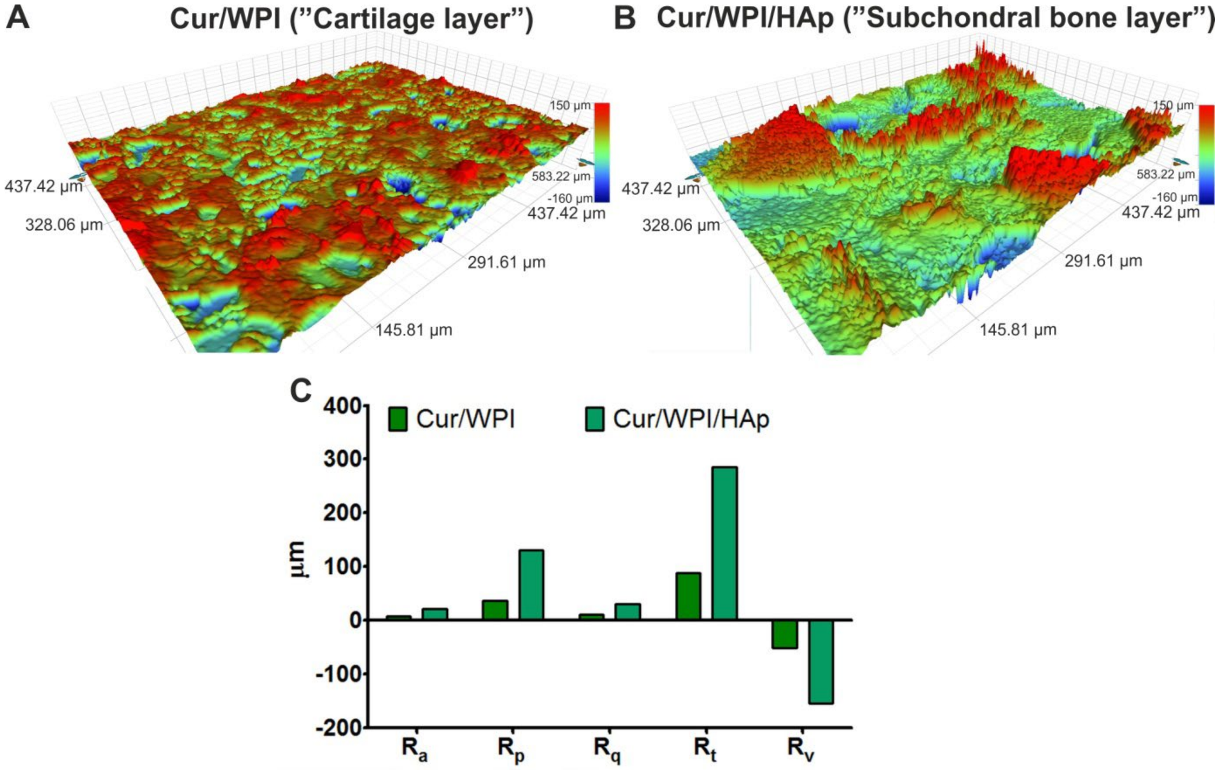

Fig. 3. The 3D optical profilometry images showing topography of the top layer (A) and the bottom layer (B) of the biphasic curdlan-based scaffold. Based on the obtained images, the following roughness parameters were calculated (Vision64 Map Software; Bruker, USA): arithmetic average height (R_a), maximum height of peaks (R_p), root mean square roughness (R_q), maximum height of the profile (R_t), and maximum depth of valleys (R_v) (C).

3.2. Identification of chemical composition of the samples by FTIR-ATR

When two or more polymers are mixed together, they can either form two separate phases (when the materials are not miscible in one another) or form a blend. A blend is a homogenous mixture of two or more compounds. A miscible blend has mechanical and thermal properties that are roughly a mean of those of the separate products. However, in some cases, when strong chemical interactions between the products appear, a blend can have these properties noticeably higher those of each of the individual separate compounds [55]. A homogenous mixture with little to no phase separation is also less likely to contain structural defects (which are a possible cause of critical failure in materials, including biomaterials). Hence, miscibility of the compounds of materials is an important factor to consider when designing new mixtures, especially if materials are to bear mechanical stresses, such as osteochondral implants. Furthermore, the compounds would ideally to be able to form strong chemical interactions with each other, further improving the mechanical properties and reducing the risk of the implant failure. FTIR spectroscopy identifies polar functional groups/chemical bonds present in the samples and as such, is a simple means to monitor appearance of chemical interactions between the compounds. Typically, this is performed by comparing the spectrum of the blend with that of the compounds. If new, IR active bonds appear in the spectrum of the blend, strong chemical interactions between the compounds can be supposed. At the same time, weak interactions (hydrogen bonds, Van der Waals interaction, or dipole-dipole interactions) can sometimes be identified by: 1) a shift in the band's wavenumber (indicative of increased strain in a certain bond due to conjugation of some of its atoms); 2) an intensity reduction (indicative of a change in the chemical environment of a certain bond, reducing its ability to vibrate upon the IR absorption, or that the overall amount of the given type of bonds has been reduced), 3) an intensity increase (which could suggest that more bonds of certain type are present in the mixture) or 4) disappearance of bands (suggesting that a vibrational degree of freedom has changed or a given functional group has decomposed). Hence, FTIR spectroscopy can be regarded as a powerful tool in characterizing new composite materials.

In this study, FTIR-ATR spectroscopy was used to evaluate the presence and the type of chemical interactions between the compounds of the scaffold. For better comparison, the compounds of the "cartilage layer" and the compounds of the "subchondral layer" of scaffold were presented on separate graphs, i.e., Fig. 4A and Fig. 4B, respectively.

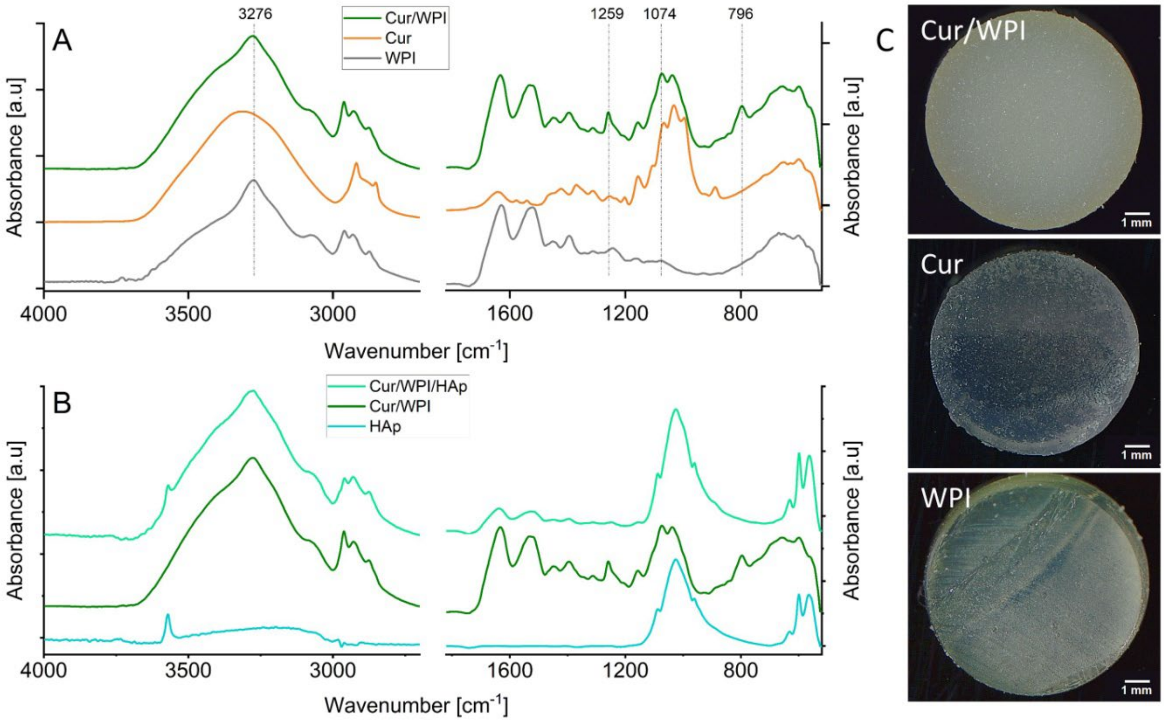

Fig 4. The FTIR-ATR spectra of the composites and their compounds: “cartilage layer” (A) and “subchondral bone layer” (B). For better clarity, the spectra are offset and maximized in two separate regions in which characteristic bands are present: from 4000 to 2700 cm^{-1} and from 1800 to 500 cm^{-1}. Stereoscopic microscope images of the compounds and the composite (C); magnification 10x, scale bar = 1 mm.

Curdlan is a polysaccharide composed of repeating units of glucose, bonded through glycosidic linkages. In this material, this glycosidic linkage exists between the hemiacetal group (anomeric carbon, C-1) of one glucose unit and the hydroxyl group of the C-3 carbon in another glucose unit. This way of bonding indicates that, in this polysaccharide, there is always one, terminal glucose moiety that can have its cyclic structure opened, recreating the aldehyde functional group. As such, curdlan is to be regarded as a reducing polysaccharide [56]. WPI, on the other hand, is a mixture of various proteins and peptides, formed of amino acids. The peptides and amino acids should also contain some amine functional groups present in their backbone. As such, WPI is expected to be rich in amine functional groups [33]. When a reducing sugar is mixed with an amine at an elevated temperature, a Maillard reaction is highly expected. WPI has already been reported to undergo a Maillard reaction upon mixing with various reducing sugars (mono-, di-, and polysaccharides): xylose, glucose, galactose, fructose, arabinose, lactose, maltose, maltodextrin, or inulin [57–59]. However, to the best of our knowledge, a reaction with curdlan has not yet been proven. Being a very complex reaction, the Maillard reaction can yield mixtures of over 100 different products which can be hard to identify unambiguously, but is has a one distinctive feature: color change [56]. In the initial stage, sugar-amine rearrangement and the Amadori rearrangement occur, and the product is transparent. Generally, amine groups from the proteins' backbone and the end units of sugar are assumed to be the first to react [60]. Progression into the intermediate stage of the reaction where the closed-chain Amadori product is formed and the sugar dehydration and fragmentation, and amino acid degradation (Strecker degradation) occur, yields an off-white to yellowish product. Further heating of the mixture gives energy for the further progression of the reaction entering into its final stage (aldol and aldehyde–amine condensations, and formation of heterocyclic nitrogen compounds), at which the product is visibly highly colored – from orange to dark brown [56]. Because the reaction can be monitored by a change of color, the product of the mixing of Cur with WPI was photographed using a stereoscopic microscope and compared with pure Cur and WPI. The results are presented in Fig. 4C.

As can be seen in Fig. 4A, the spectrum of Cur shows features characteristic of polysaccharides, similar to the ones reported in our previous studies [61,62]: a broad band at 3315 cm^{-1}, attributed to stretching of OH functional groups, abundant in its structure; a triplet between 2919 and 2852 cm^{-1}, characteristic of C-H stretching in alkanes, a band attributed to C=O stretch found at 1637 cm^{-1}, and a strong intensity triplet with maxima at 1066, 1025, and

996 cm^{-1}, attributed to C-O-C (glycosidic bond) and C-C and C-O stretching in a pyranoid ring [63], respectively. As is visible in Fig. 4C, pure and unmodified Cur is transparent.

The spectrum of WPI is characterized by a sharper band at 3276 cm^{-1} (compared to Cur) due to the presence of amide bonds [64,65], a shoulder at 3070 cm^{-1} arising from the presence of alkynes, and numerous bands between 1631 and 900 cm^{-1}, arising from the presence of various double (1630-1500 cm^{-1}), and single bands (below 1500 cm^{-1}) between carbon and oxygen, nitrogen and hydrogen (the region between 1500-1200 cm^{-1} has bands characteristic of amide III bonds). Most notably, there is a band at 1630 cm^{-1}, due to C=O stretching (amide I), and at 1524 cm^{-1}, attributed to amide II functional groups (N-H bend and C-N stretch). Similarly to Cur, pure WPI is also transparent (Fig. 4C).

As visible in Fig. 4C, Cur/WPI composite is a non-transparent, off-white solid, giving first indications that the intermediate stage of Maillard reaction likely took place. The spectrum of the Cur/WPI bears all the features characteristic of both compounds, with some additional unique observable characteristics. First of all, there are some alterations in the bands attributed to the amide I, II and III vibrational modes which are indicative of changes in the structure of WPI. Amide I/ amide II ratio is increased from 1 in WPI to 1.1 in Cur/WPI which is indicative of a higher proportion of C=O bonds in the latter sample, probably due to presence of sugars. A band at 1243 cm^{-1} in WPI and at 1254 cm^{-1} in Cur is shifted towards higher wavenumbers (1259 cm^{-1}) in Cur/WPI and has its relative intensity significantly increased. In this region, bands originate from a mixture of several coordinate displacements (amide III), including C-N-H bend, C-N stretch, and different functional groups involving C-O-C or C-O bonds (especially in phenols). It can be suggested that higher amounts of these bonds are present in the composite than were in the protein and polysaccharide and that the atoms forming these bonds might be polarized [66], strengthening the bond and causing a blue shift of its wavenumber. These observations might be indicative of the occurrence of ring opening reactions or the Amadori rearrangement taking place. In a study by Cheng et. al. [67], Maillard reaction occurring between rice protein (RP) and dextran resulted in a disappearance of 1240 cm^{-1} band found in the RP spectrum. It was explained that amine groups “were consumed during the glycation reaction”. This explanation is only partially correct as not all of the N-H bonds should disappear in the course of the reaction (Fig. 5).

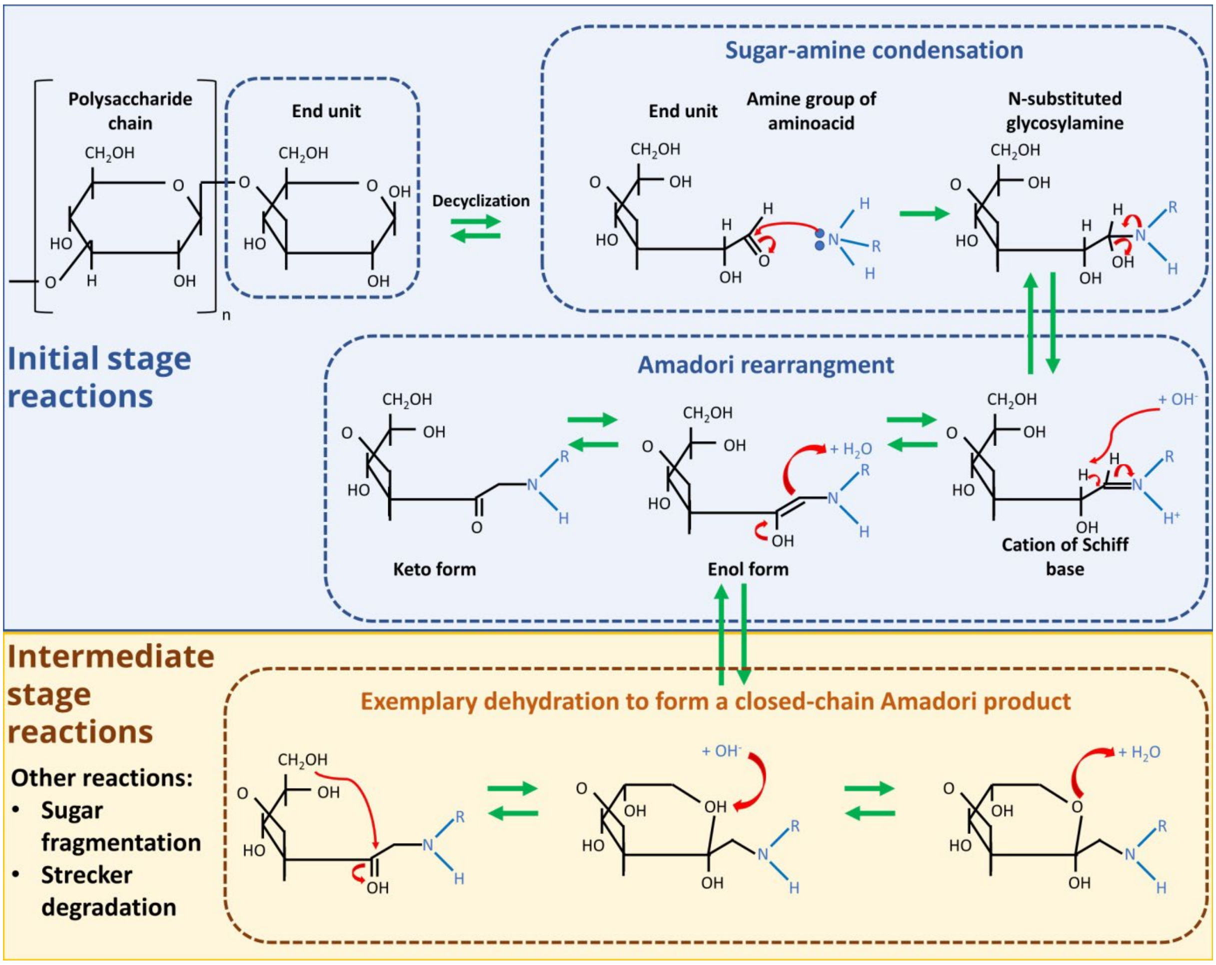

Fig 5. Some examples of the initial and intermediate stages of the Maillard reaction. The saccharides are presented in the Haworth projection. Only the end, reducing unit of the polysaccharide chain is shown during the reaction, but more units having the aldehyde functional group can be formed in the course of the process through chain and sugar fragmentation. In real life conditions, the reaction is known to yield more than 100 different products [56].

Next, it can be observed that a triplet, visible in the spectrum of Cur which is characteristic of glycosidic bonds, is substituted by a doublet, with the band at 996 cm^{-1} observably diminished. As suggested by Sinyayev et al. [68], the complex band of the glycosidic bond consists of three components of different wavenumbers, and the low-frequency one is indicative of the C-O-C bridging bonds. Hence, the intensity of this band is inversely proportional to the polymerization degree of the polysaccharide (i.e., the chain length). It can thus be suggested that sugar fragmentation involving intermolecular glycosidic bonds (β-(1,3)) has occurred in the Cur/WPI composite.

The final distinctive feature of the spectrum of the composite is the high-intensity band at 796 cm^{-1}, which is not observed in either spectrum of the components. This band should be attributed to C-H out-of-plane deformation in aldehydes or N-H deformation vibrations in amines. Hence, this could indicate reactions involving ring opening and/or decomposition of amide bonds.

It is important to know that there are many studies which aim to identify the occurrence of the Maillard reaction via FTIR analysis. Probably, one of the most significant is the study by Ioannou et al. [60]. However, translation of these results to our study is poor because we analyzed a mixture of products, by-products and reactants, while the cited article used product fractioning to monitor what was synthesized in the given temperature range. In many other studies, the spectrum of the composite material is not compared with the spectrum of the saccharide, making such analysis prone to misinterpretation [59,69–72]. Still, there are some articles that perform comparisons similar to ours, but the observed changes are different from the ones we report herein. In a recent study by Cheng et al. [67], the spectrum of a RP-dextran composite was compared with that of RP and dextran and the only difference observed was the disappearance of the 1241 cm^{-1} band. All other bands were attributed to the presence of the compounds. A different analysis performed by Wang et al. [57], indicated that the reaction of WPI with xylose or glucose led to decreased intensities of the amide I, II, and III attributed bands, and increased the amount of bands in the 1050–950 cm^{-1} region. However, it is important to note that the analyzed spectra had not been normalized before their relative intensities were compared, which may lead to deductive errors. Probably one of the most noticeable changes in the FTIR spectrum were the ones reported by Yang et al. [73]. In this study, a reaction between soy protein isolate and soy soluble polysaccharide had resulted in the appearance of a new band at 1660 cm^{-1}, which the authors attributed to the formation of Schiff's base product – either imine or enaminol. However, it is important to be aware of the fact that the 1660 cm^{-1} band is characteristic of the C=O bond stretch, especially not bonded, and hence, the presence of imine should rather be excluded. Instead, such splitting of the C=O band into two (wherein the one of lower wavenumber is attributed to amides, and a new one at higher wavenumbers indicates a free carbonyl group), should rather be interpreted by the formation of aldehyde or ketone functional groups – hallmarks of the Amadori rearrangement. The authors also suggested changes in the amide II and amide III region, but we find these implications questionable given the high noise level of the spectra presented.

In summary, because the two compounds of the composites were polysaccharides and proteins, the fabrication process was conducted at elevated temperatures (90°C), and FTIR-ATR analysis suggested reactions involving N-H and C-H bonds, it is highly probable that a Maillard reaction took place [36]. Based solely on FTIR analysis it is impossible to unambiguously identify the reaction products, especially due to the fact that most of the products will have spectral modes present in the similar regions which will also overlap with those of the unreacted products [60]. However, this was not the aim of this analysis and instead, the goal was to investigate whether strong chemical interactions exist in the as-prepared polymer blend. As the obtained product is off-white, final stages of Maillard reactions should be excluded; however, as supported by the FTIR analysis, initial and intermediate stages are highly probable. Reactions capable of inducing the observed changes in the spectrum of Cur/WPI can be suggested. An increase in the overall amount of IR-active C-O groups (at 1259 cm^{-1}) can be induced by sugar decyclization and fragmentation, or partial loss of tertiary and secondary structure of proteins in WPI (breaking of the hydrogen bonds). A reaction involving formation of new N-H/C-H bonds (at 796 cm^{-1}) could be creation of N-substituted glycosylamines, decomposition of peptide bonds or saccharide decyclization. C-H/N-H bonds created at these stages would remain present in most products that follow. Additionally, fragmentation of the polysaccharide chain could be suggested (diminishing of the 996 cm^{-1} band).

To sum up, the as-performed analysis suggests the presence of strong interactions between the biopolymers which could contribute to improved mechanical properties and stability of the obtained material.

The spectra of the "subchondral layer" and its compounds are given in Fig. 4B. It can be seen that the spectrum of HAp is typical of this inorganic material, with a band at 3573 cm^{-1} arising from the stretching vibrations of the lattice hydroxyl ions, a triplet at 1088, 1026, and 961 cm^{-1} arising from the stretching of the P-O bond, a band at 632 cm^{-1}, attributed to bending in the OH groups, and a doublet at 599, and 565 cm^{-1}, arising from the O-P-O bending modes [74]. Mixing HAp with Cur/WPI results in a spectrum that is mostly a sum of the compounds, but still, there are some alterations visible, mainly as changes in intensity. In HAp, the absolute intensity ratio of the 3573 cm^{-1} to the 1026 cm^{-1} band was 0.03, while mixing with biopolymers resulted in a reduction of this ratio to 0.01. This indicates that there was a chemical interaction between the OH^{-} ions of HAp and the functional groups of the biopolymer. To better analyze which functional groups of the Cur/WPI participated in these interactions, its spectrum and that of Cur/WPI/HAp were normalized to the bands at 1638 cm^{-1} and 1526 cm^{-1} and the resultant, selected spectral regions are presented in Fig. 6.

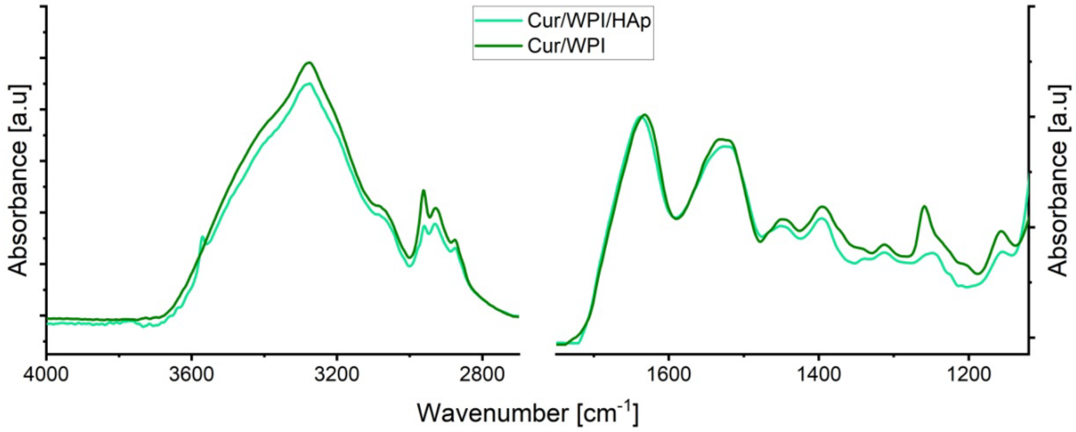

Fig 6. The FTIR-ATR spectra of the "subchondral bone layer" and its biopolymeric compound. The spectra are normalized in the 1715 – 1475 cm^{-1} region and are presented in the two spectral regions: from 4000 to 2700 cm^{-1} and from 1800 to 1120 cm^{-1}.

Overall, interaction with HAp resulted in a decreased intensity of the complex OH/NH-attributed band at 3276 cm^{-1}, which might indicate chemical interactions involving these groups (probably a hydrogen bridging). There is also a reduced signal from the C-H stretch of saturated alkanes which is visible in the 3000 - 2700 cm^{-1} region, which suggests reduced resonation of the biopolymer's backbone, indicative of chemical interactions concerning the side-chain functional groups. Similarly, there is also a reduction in the overall intensity of the amide III attributed bands (below 1480 cm^{-1}), which is particularly visible due to a significant reduction of the band visible at 1259 cm^{-1}, which is also connected with its downshift towards the lower wavenumbers 1249 cm^{-1}. As already suggested, this band likely originates from different functional groups involving C-O-C bonds or C-O (especially in phenols). Its diminishing suggests chemical interaction involving these groups, likely a hydrogen bridging with the hydroxyl groups of HAp, which also depolarizes atoms (previously polarized during the Maillard reaction), causing a red-shift of the band (towards lower wavenumbers). Finally, a small band which appeared in the reaction between the sugar and the protein (at 796 cm^{-1}) is no longer visible upon mixing with HAp. This band has been suggested to originate from the C-H out-of-plane deformation in aldehydes or N-H deformation vibrations in amines. Since this band is absent in the Cur/WPI/HAp, a complete consumption of these functional groups is suggested. At this stage, the particular reaction is hard to identify, but based on the chemical composition of the material used, a formation of hemiacetal seems plausible. Based on the presented analysis, the Cur/WPI/HAp could be classified as a class I hybrid, but it cannot be excluded that it is, in fact, a class II hybrid [75,76]. Presence of chemical interactions between the compounds is highly favorable when the material is intended for use as an osteochondral implant, as hybrids should be characterized by improved thermal and mechanical properties and improved stability.

3.3. Young's modulus of biomaterial

Mechanical tests revealed that the Cur/WPI biomaterial possessed the lowest value (1.07 ± 0.13 MPa, $P > 0.05$) of Young's modulus (E) as compared to the other two samples (Fig. 7 A,B). The presence of HAp granules in Cur/WPI/HAp biomaterial resulted in an improvement of the mechanical properties ($E=1.17 \pm 0.21$ MPa), but surprisingly, the difference was not statistically significant. Presumably, this phenomenon is associated with the very small diameter of HAp granules (0.05-0.2 mm). As a consequence, their addition did not significantly influence the mechanical properties of Cur/WPI biomaterial. Thus, HAp granules of varying sizes will be tested in future in order to find the right size range for the improvement of mechanical properties – it is possible that two or more fractions of different sizes would be more optimal than just a single one. It is worth noting that addition of ceramic particles to hydrogels is a common approach to mineralize hydrogels [77]. For example, previous studies involving addition of aragonite particles to WPI hydrogels revealed an increase in Young's modulus with increasing aragonite particle concentration up to 30% (w/v)

[30]. However, addition of particles to WPI hydrogels does not automatically result in mechanical reinforcements. Another previous study involving addition of 10% and 20% (w/v) of bioactive glass particles to WPI hydrogels revealed decreases in Young's modulus [31]. The highest mean E value was determined for the biphasic scaffold (1.28 ± 0.20 MPa), but it was also similar ($P > 0.05$) to those of Cur/WPI and Cur/WPI/HAp biomaterials. These results suggested that all the tested biomaterials exhibited comparable mechanical properties.

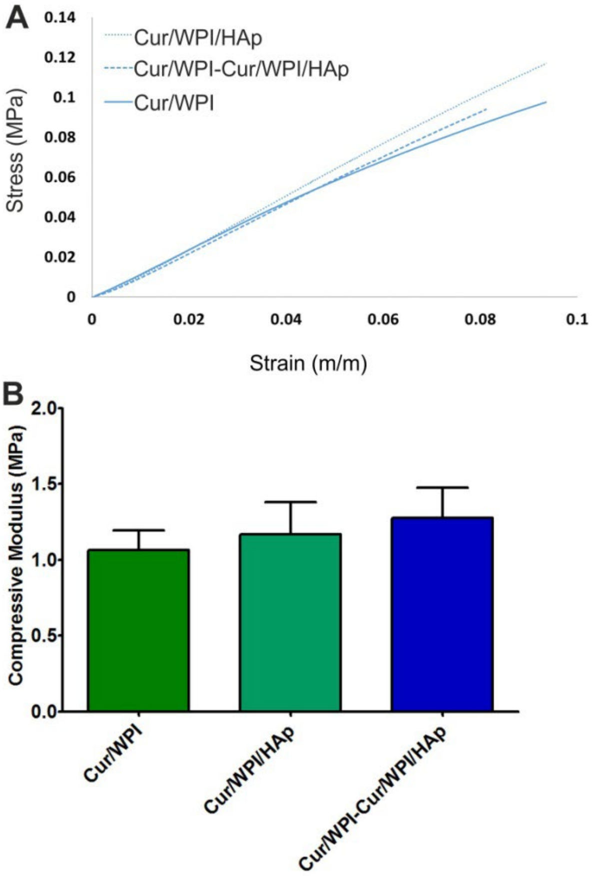

Fig. 7. Stress-strain curves (A) and Young's modulus values (B) for the investigated biomaterials: Cur/WPI, Cur/WPI/HAp and biphasic Cur/WPI-Cur/WPI/HAp. The results were obtained using 5 separate biomaterials (*n*=5). The differences between samples were not statistically significant.

Given the structure and composition of cartilage and subchondral bone, it is known that these tissues possess different mechanical properties. According to the available data

[9,15,78], mean values of Young's modulus (E) are between 0.08 and 2.00 MPa for cartilage and between 11.12 and 15.33 GPa for the subchondral bone. Thus, the Young's modulus value determined for the top layer (Cur/WPI) of the curdlan-based scaffold was close to that of native cartilage, while the E value obtained for the bottom layer (Cur/WPI/HAp) of scaffold was significantly lower when compared to that of natural subchondral bone. Nevertheless, it is worth underlining that fabrication of biomaterials which combine mechanical properties similar to those of cartilage and subchondral bone simultaneously remains challenging. For instance, Parisi et al. developed a biomimetic osteochondral scaffold composed of collagen and hydroxyapatite, and they demonstrated that its E value ranged for 0.006 to 0.02 MPa [18]. Xiao et al. fabricated osteochondral silk fibroin-chitosan-nanohydroxyapatite scaffolds with E values in the range of 0.095-0.347 MPa [79]. In turn, Liu et al. developed a biomimetic bilayered collagen-hyaluronic acid-nanohydroxyapatite scaffold for osteochondral tissue repair. They showed that the values of Young's modulus for a single layer (collagen-hyaluronic acid) and a bilayer composite (collagen-hyaluronic acid-nanohydroxyapatite) were approx. 0.087 and 0.212 MPa, respectively [49]. Thus, taking into consideration the results obtained by other authors, the fabricated biphasic curdlan-based scaffold seems to be a promising biomaterial for osteochondral tissue engineering. However, in future, we plan to modify this biomaterial in order to improve its mechanical properties.

3.4. Swelling ability

The water uptake assay demonstrated that the biphasic Cur/WPI-Cur/WPI/HAp biomaterial possessed a slight ability to swell (Fig. 8). After 25 min. of soaking the percentage increase of its weight reached approx. 3% and at this time sorption equilibrium was achieved. The swelling ability is a very significant property of implantable biomaterials. It allows to determine the time needed during the pre-operative procedure, as a surgeon usually wets biomaterials in 0.9% NaCl solution or antibiotics before implantation. If a biomaterial swells at the implantation site, it exerts pressure on the surrounding tissues and as a consequence it leads to local inflammation. In many cases such implants must be removed [25]. According to our knowledge obtained during conversations with surgeons, the time needed for complete saturation of the biomaterial should not be longer than 30 minutes. The Cur/WPI-Cur/WPI/HAp biomaterial achieved complete saturation below this time, thus it seems that its application as implantable biomaterial is not limited.

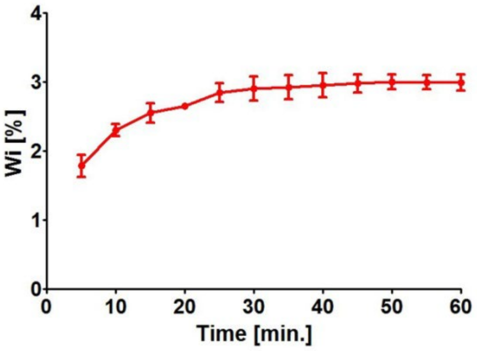

Fig. 8. Swelling ability of the biphasic Cur/WPI-Cur/WPI/HAp biomaterial. It was presented as an increase in its weight (Wi) after soaking in 0.9% NaCl solution.

3.5. Ion-release assay

In order to determine the influence of our curdlan-based scaffold on the culture medium composition, a 15 day long experiment was performed. This assay was carried out because some biomaterials possess an ability to release/adsorb ions (e.g., calcium or phosphate ions) to/from a culture medium, which in consequence can have either beneficial or unfavorable effects on the cell viability, proliferation, and differentiation *in vitro* [26,38,80,81]. The performed analysis demonstrated that the Cur/WPI biomaterial did not possess the ability to change the concentration of Ca^{2+} ions in the culture medium during the whole duration of the experiment (Fig. 9A). In turn, the Cur/WPI/HAp biomaterial released significant amounts ($P < 0.05$) of Ca^{2+} ions until 12 days. On the 15th day of incubation, a relatively high decrease in concentration of Ca^{2+} ions was observed, which suggests that the

Cur/WPI/HAp biomaterial adsorbed these ions from the culture medium. A similar tendency was noted in the case of HPO_4^{2-} ions' concentration (Fig. 9B). For 12 days of incubation, the Cur/WPI/HAp biomaterial released significant amounts of these ions (apart from the third day), while the Cur/WPI sample did not have an influence on HPO_4^{2-} ion concentrations. However, on the 15th day of incubation, both biomaterials exhibited ability to absorb significant amounts ($P < 0.05$) of these ions from the culture medium. The observed increase in Ca^{2+} and HPO_4^{2-} ions concentrations in the culture medium up to 12 days of Cur/WPI/HAp biomaterial incubation was most likely associated with the dissolution of HAp granules. This phenomenon should have a beneficial effect on *in vitro* cytocompatibility and bioactivity of this biomaterial. Calcium ions play a crucial role in cell metabolism, thus scaffolds possessing the ability to release these ions can (up to a certain concentration), support stem cell viability, migration, proliferation, and chondrogenic as well as osteogenic differentiation [82–84]. It was demonstrated that an extracellular concentration of Ca^{2+} ions *in vitro* up to 1.8 mM (72 mg/L) promotes both chondrogenic and osteogenic differentiation of stem cells, while a higher concentration of Ca^{2+} ions (approx. 8mM, i.e., 320 mg/l) inhibits chondrogenic differentiation of stem cells without unfavorable effects on osteogenic differentiation of these cells [85]. In our study, the highest concentration of Ca^{2+} ions released by Cur/WPI/HAp (on the third day) was approx. 12 mg/l (0.3 mM). Thus, this concentration should enable both chondrogenic and osteogenic differentiation of stem cells *in vitro* and should not be toxic *in vivo*. It was found that during osteoclast-mediated bone resorption *in vivo*, the extracellular concentration of Ca^{2+} at damage zones of bone may range from 9 mM up to 180 mM (360-7200 mg/l) [86]. Moreover, an increase in the concentration of Ca^{2+} and HPO_4^{2-} ions in the surrounding environment of a biomaterial promotes a successive *in vitro* apatite formation on its surface [26,38,41]. It is likely that the apatite crystals started to be formed from the 12th began to absorb both Ca^{2+} and HPO_4^{2-} ions from the culture medium.

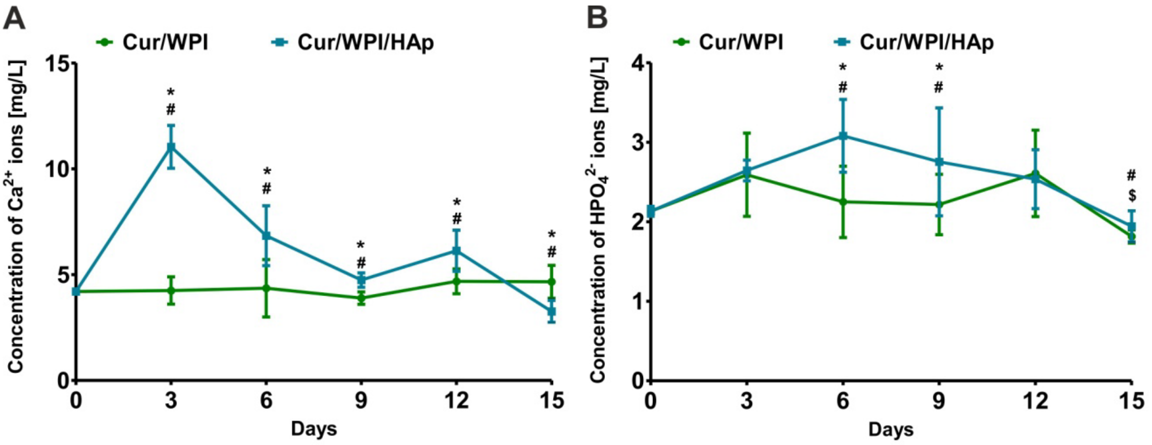

Fig. 9. Ion-reactivity of Cur/WPI and Cur/WPI/HAp biomaterials. The changes in concentration of Ca^{2+} (A) and HPO_4^{2-} (B) ions in the culture medium were evaluated during 15-day incubation. * Statistically significant differences between concentration of ions in the culture medium after incubation with Cur/WPI and concentration of ions in the culture medium after incubation with Cur/WPI/HAp; $^{\$}$ Statistically significant differences between concentration of ions in the culture medium after incubation with Cur/WPI and concentration of ions in the culture medium before incubation (day 0); $^{\#}$ Statistically significant differences between concentration of ions in the culture medium after incubation with Cur/WPI/HAp and concentration of ions in the culture medium before incubation (day 0), according to an One-Way ANOVA test followed by Tukey’s multiple comparison, $P < 0.05$.

3.6. *In vitro* biocompatibility with stem cells

3.6.1. Assessment of cell adhesion and spreading

After 48-h incubation of the biomaterials with cells, confocal microscope images (Fig. 10) demonstrated that surfaces of both Cur/WPI and Cur/WPI/HAp biomaterials promoted the adhesion of both stem cell types (ADSCs and BMDSCs). The ADSCs and BMDSCs grown on Cur/WPI and Cur/WPI/HAp were flattened and possessed a well-developed system of cytoskeletal filaments (Fig. 10).

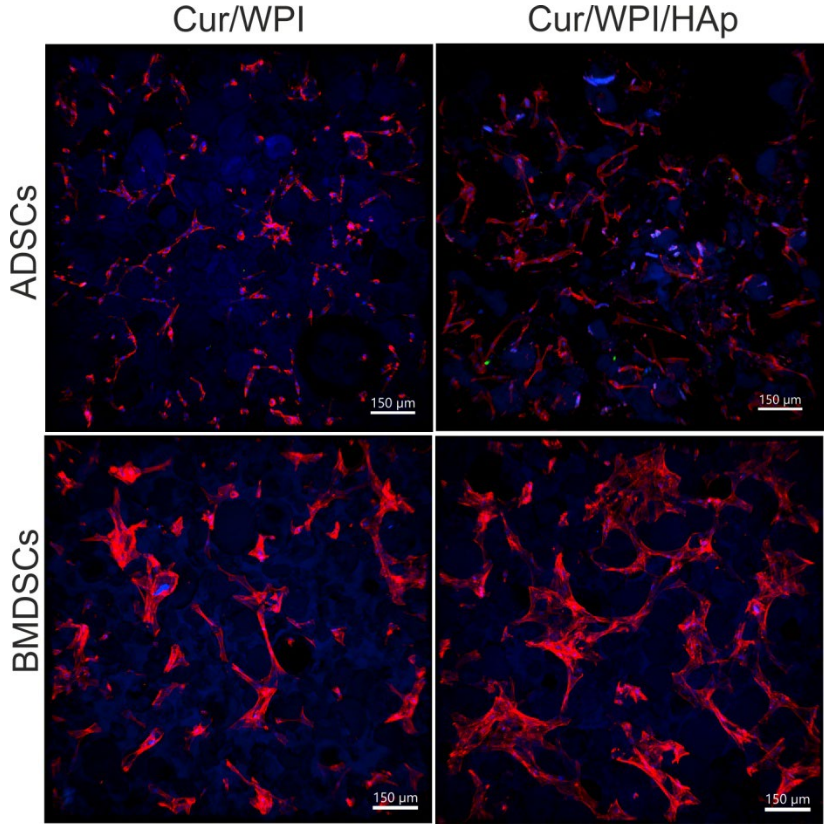

Fig.10. Confocal microscope images demonstrating adhesion of human adipose tissue-derived mesenchymal stem cells (ADSCs) and human bone marrow-derived mesenchymal stem cells (BMDSCs) to the surface of Cur/WPI and Cur/WPI/HAp biomaterials. Nuclei – blue fluorescence, F-actin – red fluorescence. Visible blue fluorescence in the structure of biomaterials was emitted by WPI; objective magnification 10x, scale bar =150 µm.

In addition, quantitative measurements confirmed that both biomaterials supported the stem cell adhesion and growth (Fig. 11). The spreading area of both ADSCs and BMDSCs was greater when the cells were grown on the Cur/WPI/HAp samples, as compared to the Cur/WPI biomaterials. Nevertheless, statistically significant differences ($P < 0.05$) were noted only for BMDSCs, with mean values of spreading area per cell equal to 16.93 ± 3.96 μm^2 on Cur/WPI, and 21.36 ± 3.76 μm^2 on Cur/WPI/HAp. Presumably, a better adhesion of both stem cell types can be associated with some specific properties of the investigated biomaterials. The Cur/WPI/HAp biomaterial exhibited a higher microscale surface roughness (Fig. 3B), when compared to the Cur/WPI biomaterial (Fig. 3B), which can increase the specific surface area on the material and can provide a larger space for cell adhesion and spreading. In addition, the Cur/WPI/HAp biomaterial possesses the ability to release a significant amount of Ca^{2+} and HPO_4^{2-} ions into the culture medium (Fig. 9 A,B), as compared to the Cur/WPI scaffold (9 A,B). It is well known that Ca^{2+} ions support the adsorption of cell adhesion-mediating proteins to the biomaterials' surface and the cell adhesion through integrin adhesion receptors [87,88].

Cur/WPI/HAp morphology was designed to mimic the native morphology of subchondral bone, which possess a hierarchically-organized macroscale, microscale, and nanoscale structure. BMDSCs, which are bone-derived cells prone to osteogenic differentiation [89,90], can be therefore expected to prefer the Cur/WPI/HAp biomaterial with hierarchically-organized surface roughness over a smoother biomaterial (Cur/WPI). Meanwhile, ADSCs, which are not primarily designed to form bone or cartilage, but are derived from adipose tissue in which extracellular matrix lacks morphological features and is not mechanically stable, do not exhibit preferences towards the particular morphology of the substrate. Moreover, these cells, even though derived from the same donor, have a lower capacity for osteogenic differentiation and they seem to be more suitable for soft tissue engineering, e.g., for adipose tissue engineering [89,90], neural tissue engineering [91], for revascularization of various tissues [92,93], or for immunomodulatory therapies [94]. Thus, the lower ability of ADSCs to adhere to Cur/WPI and Cur/WPI/HAp biomaterials, when compared to BDMSCs, is probably because neither of the materials are able to mimic the natural environment of ADSCs, and the cells are generally reported to grow better on scaffolds that share similar characteristics to those of their natural environment [95,96].

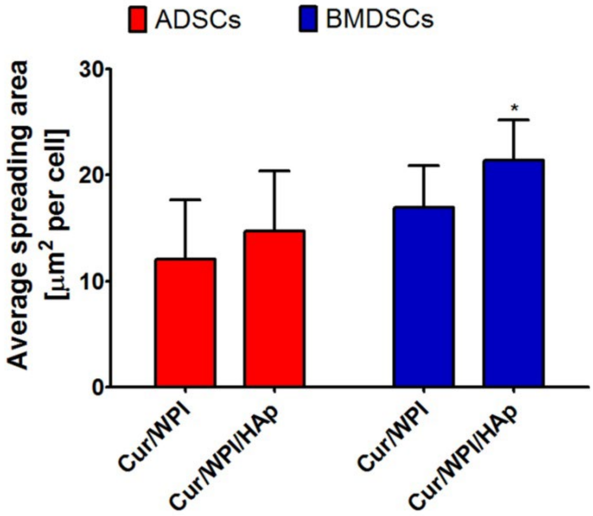

Fig.11. Quantification of the spreading area of human adipose tissue-derived mesenchymal stem cells (ADSCs) and human bone marrow-derived mesenchymal stem cells (BMDSCs) after 48-hour culture on the surface of Cur/WPI and Cur/WPI/HAp biomaterials. The results were expressed as average value of spreading area [μm^2] per one cell. * Statistically significant differences compared to the Cur/WPI biomaterial, according to One-way ANOVA test followed by Tukey's multiple comparison, $P < 0.05$.

3.6.2. Assessment of cell proliferation

The resazurin test revealed that all the tested biomaterials (polystyrene – PS, Cur/WPI, and Cur/WPI/HAp) promoted stem cell proliferation during the experiment (Fig. 12). The metabolic activity of stem cells grown on PS (control) was higher compared to the metabolic activity of stem cells cultured on Cur/WPI and Cur/WPI/HAp samples, but it was an expected result, as the cells grown in 3D conditions (on biomaterials) require more time for adjustment and to commence division compared to cells cultured in 2D conditions (on PS) [43]. Nevertheless, the metabolic activity of stem cells cultured on the tested biomaterials increased with the time (apart from cells cultured on Cur/WPI for 2- and 5 days). Thus, after 8-day culture, it was observed that the Cur/WPI and Cur/WPI/HAp scaffolds supported stem cell proliferation. In the case of ADSCs, it was observed that the Cur/WPI/HAp scaffold more potently supported the cell division (except on the 2nd day of incubation), as compared to the Cur/WPI biomaterial. Nevertheless, statistically significant results ($P < 0.05$) between these two biomaterials were noted only on the 8th day of the experiment. In turn, BMDSCs proliferated in a similar manner on both investigated biomaterials on the 2nd and the 8th day of incubation, while on the 5th day of culture, significant differences ($P < 0.05$) between scaffolds were observed, with more cells observed on Cur/WPI/HAp. Thus, this experiment confirmed the results obtained previously (Section 3.6.1) and proved that both Cur/WPI and Cur/WPI/HAp supported adhesion, spreading, and proliferation of stem cells. Both cell types were found to exhibit a slight preference towards the Cur/WPI/HAp, possibly due to higher roughness found on this material (Fig. 3B,C), which may have positively affected the cellular viability.

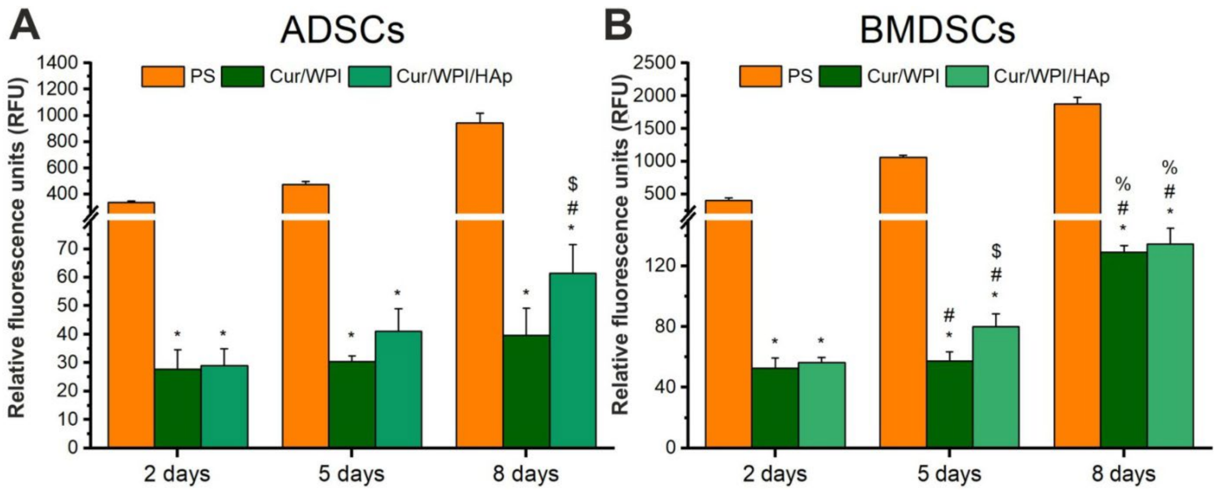

Fig.12. Proliferation of human adipose tissue-derived mesenchymal stem cells (ADSCs) (A) and human bone marrow-derived mesenchymal stem cells (BMDSCs) (B) after 2-, 5-, and 8-day culture on the polystyrene (PS, control) and surface of Cur/WPI and Cur/WPI/HAp biomaterials. The results were obtained using the resazurin assay.* Statistically significant differences compared to control (PS); $^\$$Statistically significant differences between Cur/WPI and Cur/WPI/HAp at specified time of incubation; $^\#$ Statistically significant differences compared to results obtained on day 2; $^\%$ Statistically significant differences compared to

results obtained on day 5; according to One-way ANOVA test followed by Tukey's multiple comparison, $P < 0.05$.

3.6.3. Assessment of cell differentiation

This experiment was performed in order to evaluate the ability of Cur/WPI and Cur/WPI/HAp biomaterials to support chondrogenic or osteogenic differentiation of stem cells, respectively. During the experiment, two different conditions were applied; either the ADSCs and BMDSCs were seeded directly on the investigated biomaterials and then incubated in the chondrogenic/osteogenic medium (marked as + supplements) or in the growth culture medium without the differentiation supplements (marked as - supplements). Such an approach allowed determination whether the biomaterials supported chondrogenic/osteogenic differentiation of stem cells under standard conditions (i.e., when the cells were cultured in supplemented media) as well as whether the scaffolds possessed chondroinductive/osteoinductive properties (i.e., when the cells were cultured in growth culture media without any supplements) [52,97–99]. Then, the cartilage-related markers (collagen II, aggrecan, and SOX-9) as well as the bone-related markers (collagen I, ALP, and osteocalcin) were visualized by immunofluorescence staining (Fig. 13, 14, 15, 16).

In the case of the Cur/WPI biomaterial, it was observed that it enabled chondrogenic differentiation of ADSCs (Fig. 13) and BMDSCs (Fig. 14) under standard conditions, i.e., when the cells were cultured in chondrogenic medium. Immunofluorescence of collagen II and SOX-9 was observed in both cell types, the latter being more intensive in the BMDSCs culture. Immunofluorescence of aggrecan was detected only for ADSCs. In the growth culture medium without supplements, the ADSCs (Fig. 13) cultured on the Cur/WPI scaffold did not possess the ability to synthesize characteristic chondrogenic markers, while the BMDSCs (Fig. 14) synthesized collagen II and SOX-9. Thus, these results may indicate that the

Cur/WPI biomaterial enabled chondrogenic differentiation under standard conditions and also may have chondroinductive properties (based on the data obtained for BMDSCs, which are bone-derived stromal cells with intrinsically higher osteogenic capacity). Moreover, it was observed that Cur/WPI supported osteogenic differentiation of ADSCs (Fig.15) and BMDSCs (Fig.16) under standard conditions, i.e., when the cells were cultured in osteogenic medium. The immunofluorescence of ALP and osteocalcin was detected in ADSCs, while strong immunofluorescence of all osteogenic markers (collagen I, ALP, osteocalcin) was observed in BMDSCs. In turn, ADSCs cultured in the growth culture medium without supplements (Fig. 15) almost did not synthesize osteogenic markers (only slight immunofluorescence of ALP was visible), while BMDSCs (Fig. 16) synthesized considerable amounts of collagen I, ALP, and osteocalcin. Thus, these results may indicate that the Cur/WPI biomaterial supported osteogenic differentiation under standard conditions and also may possess osteoinductive properties (based on the data obtained for BMDSCs, which are bone-derived stromal cells with intrinsically higher osteogenic capacity).

In turn, cell culture on the Cur/WPI/HAp biomaterial revealed that this scaffold promoted chondrogenic differentiation of ADSCs (Fig. 13) and BMDSCs (Fig. 14) not only under standard conditions (in medium with supplements), but also when the cells were cultured in growth medium without osteogenic supplements. Hence, immunofluorescence of collagen II, aggrecan, and SOX-9 was observed in all tested variants of cell culture on Cur/WPI/HAp (Fig.13, 14). These results clearly indicated that the Cur/WPI/HAp biomaterial supported chondrogenic differentiation of ADSCs and BMDSCs as well as possessing chondroinductive properties. Additionally, this scaffold allowed osteogenic differentiation of stem cells both in the supplemented medium as well as when the cells were incubated in the growth medium without supplements (i.e., possessed osteoinductive properties). Both ADSCs (Fig. 15) and BMDSCs (Fig. 16) exhibited ability to synthesize all the investigated markers –

collagen I, ALP, and osteocalcin, with higher amounts observed in the BMDCs culture. This phenomenon seems to be associated with structural and physicochemical features of this biomaterial. As mentioned above, the Cur/WPI/HAp biomaterial possessed a rougher structure and had the ability to release significant amounts of Ca^{2+} and HPO_4^{2-} ions to the culture medium, as compared to the Cur/WPI scaffold. This biomaterial can also be regarded as highly biomimetic (morphologically and chemically) to the bone tissue, thus potentially affecting the cellular behavior. It is worth noting that our observations are in good agreement with the results demonstrated by other researchers. It was shown that BMDSCs possessed increased chondrogenic and osteogenic capacity, when compared to ADSCSs [39,89,90,100,101]. For instance, Xie et al. [101] fabricated a scaffold composed of platelet-rich plasma (PRP) and then compared chondrogenic differentiation of ADSCs and BMDSCs in direct contact with this biomaterial. The authors indicated that such a scaffold enabled chondrogenic differentiation of both types of cells, while BMDSCs exhibited higher expression of cartilage-specific genes, when compared to ADSCs. In turn, Przekora et al. [39] compared osteogenic differentiation of ADSCSs and BDMSCs cultured on a chitosan/β-1,3-glucan/HAp biomaterial. The authors demonstrated that both type of cells possessed the ability to undergo osteogenic differentiation, but the osteogenic capacity of BMDSCs was greater than those of ADSCs. Similarly, Mohamed-Ahmed et al. [90] cultured stem cells on poly(l-lactide-co-ε-caprolactone) scaffolds and demonstrated higher osteogenic differentiation of BDMSCs, when compared to ADSCs.

In summary, according to the confocal microscope observations, the Cur/WPI and Cur/WPI/HAp scaffolds revealed an ability to support the chondrogenic and osteogenic differentiation of stem cells. In both cases, differentiation without supplementing the media was observed in the bone-derived cell type, BMDSCs, indicating higher potential of these cells to be applied in tissue engineering of the osteochondral defects. It is worth noting that differentiation of cells may be evaluated using various methods, i.e., immunofluorescence staining [39], histochemical staining [102], ELISA tests [25], RT-qPCR analysis [103], Western blotting [104] etc. Thus, based on our preliminary results using the immunofluorescence staining, it seems that the Cur/WPI and Cur/WPI/HAp may be considered as promising biomaterials for osteochondral defect regeneration. In future, we plan to perform additional analyses, enabling quantification of the studied differentiation markers, in order to confirm the chondroinductive and osteoinductive properties of Cur/WPI and Cur/WPI/HAp biomaterials.

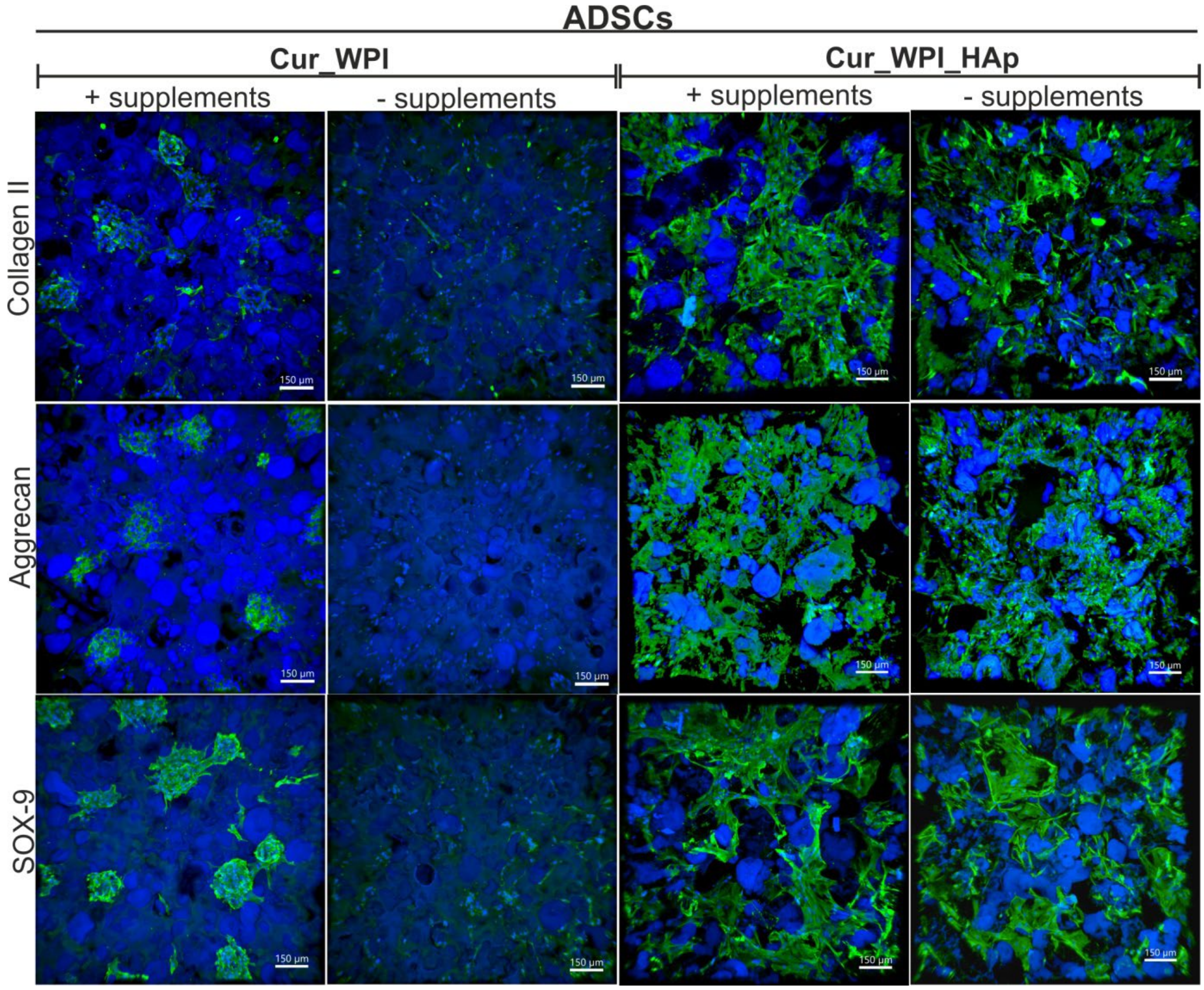

Fig. 13. Confocal microscope images demonstrating chondrogenic differentiation of human adipose tissue-derived mesenchymal stem cells (ADSCs) after 15-day culture on the surface of the Cur/WPI and Cur/WPI/HAp biomaterials. The cells were cultured in the chondrogenic

medium (+ supplements) or in the growth culture medium (- supplements). Nuclei – blue fluorescence, collagen II; aggrecan; SOX-9 – green fluorescence. Visible blue fluorescence in the structure of biomaterials was emitted by WPI; objective magnification 10x, scale bar =150 μm.

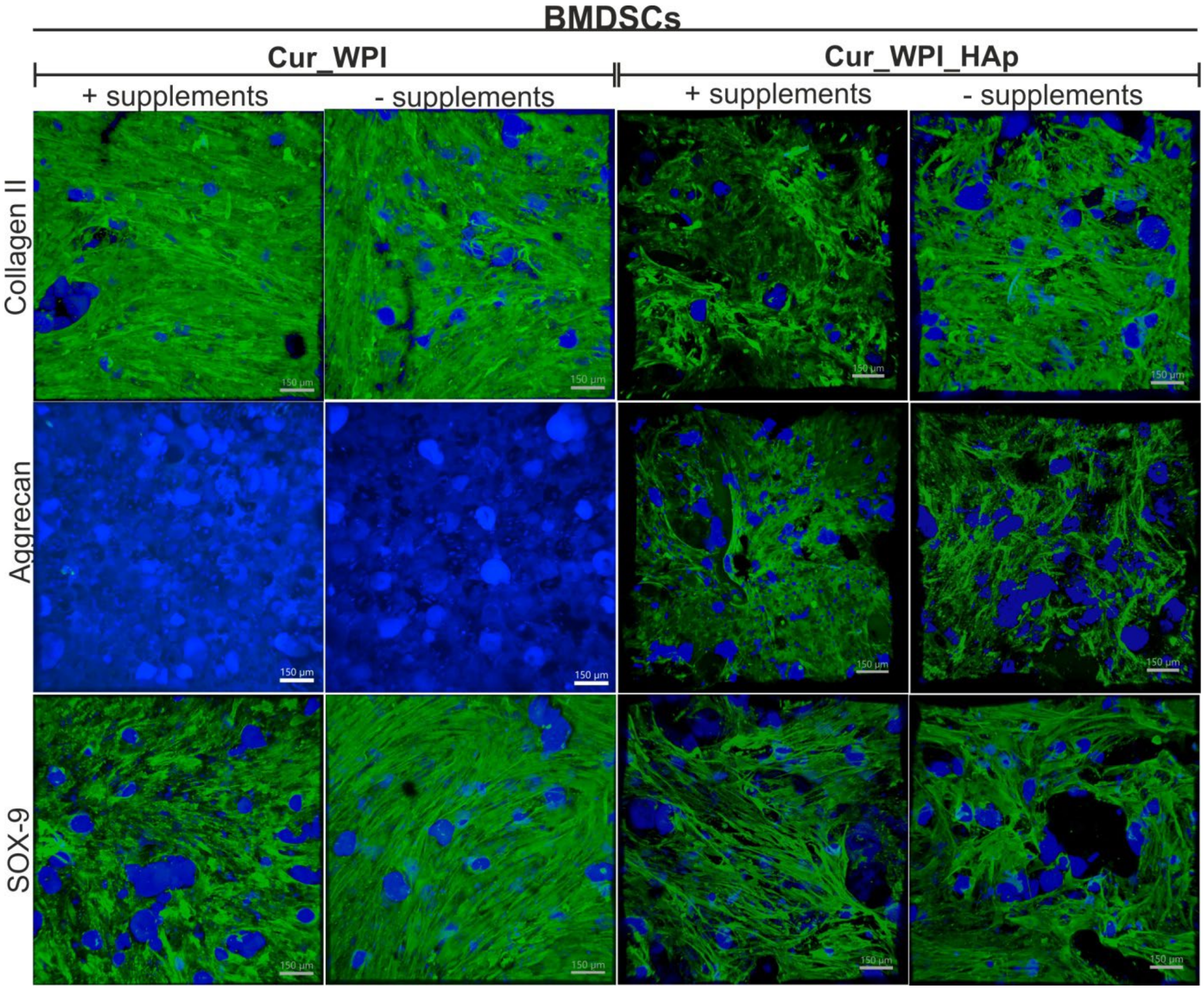

Fig. 14. Confocal microscope images demonstrating chondrogenic differentiation of human bone marrow-derived mesenchymal stem cells (BMDSCs) after 15-day culture on the surface of the Cur/WPI and Cur/WPI/HAp biomaterials. The cells were cultured in the chondrogenic medium (+ supplements) or in the growth culture medium (- supplements). Nuclei – blue fluorescence, collagen II; aggrecan; SOX-9 – green fluorescence. Visible blue fluorescence in the structure of biomaterials was emitted by WPI; objective magnification 10x, scale bar =150 μm.

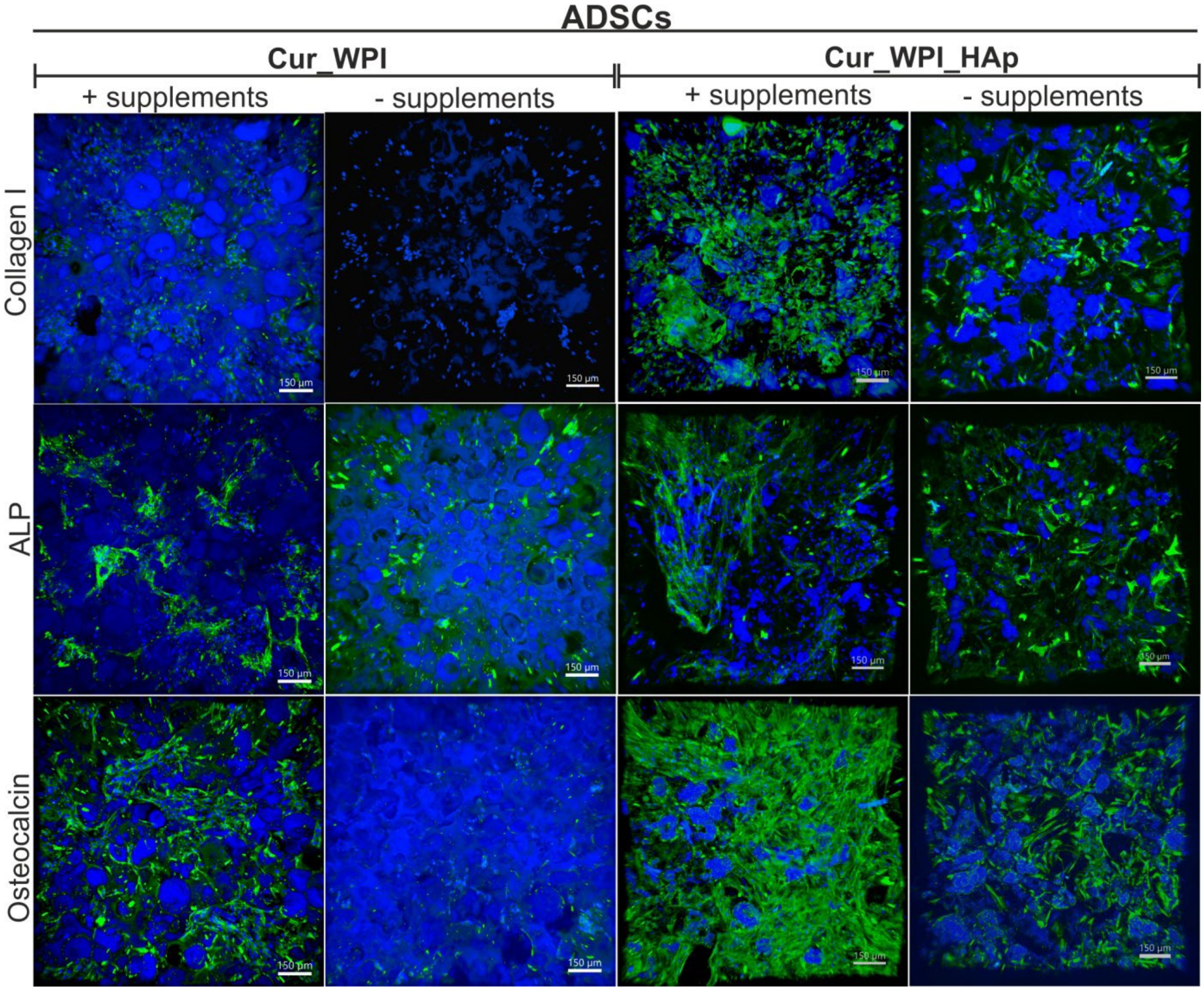

Fig. 15. Confocal microscope images demonstrating osteogenic differentiation of human adipose tissue-derived mesenchymal stem cells (ADSCs) after 15-day culture on the surface of the Cur/WPI and Cur/WPI/HAp biomaterials. The cells were cultured in the osteogenic medium (+ supplements) or in the growth culture medium (- supplements). Nuclei – blue fluorescence, collagen I; alkaline phosphatase (ALP); osteocalcin – green fluorescence. Visible blue fluorescence in the structure of biomaterials was emitted by WPI; objective magnification 10x, scale bar =150 µm.

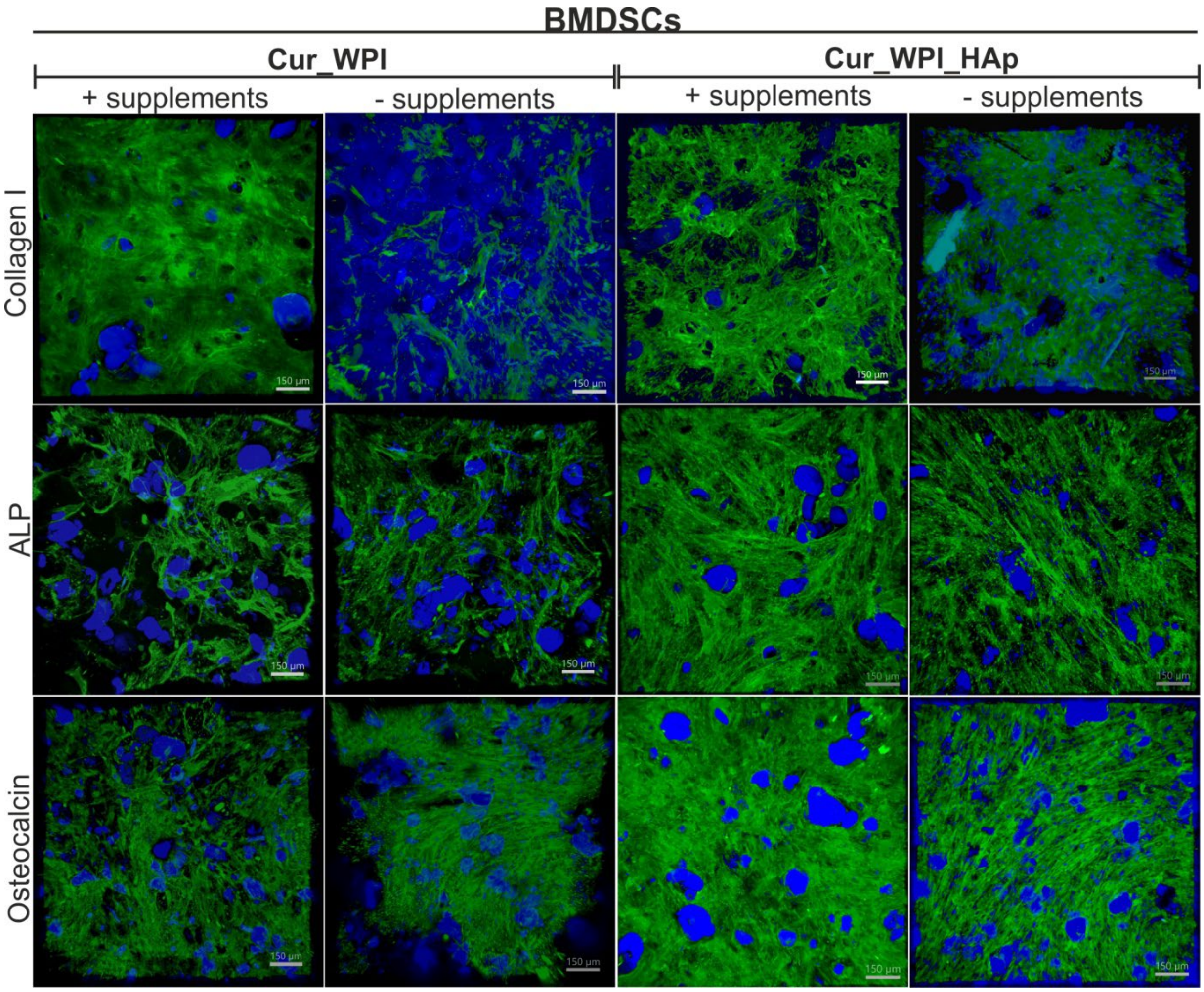

Fig. 16. Confocal microscope images demonstrating osteogenic differentiation of human bone marrow-derived mesenchymal stem cells (BMDSCs) after 15-day culture on the surface of the Cur/WPI and Cur/WPI/HAp biomaterials. The cells were cultured in the osteogenic medium (+ supplements) or in the growth culture medium (- supplements). Nuclei – blue fluorescence, collagen I; alkaline phosphatase (ALP); osteocalcin – green fluorescence. Visible blue fluorescence in the structure of biomaterials was emitted by WPI; objective magnification 10x, scale bar =150 µm.

4. Conclusions

In this study, a novel curdlan-based scaffold for osteochondral tissue engineering was fabricated and characterized *in vitro*. The performed analyses showed that the individual phases of the biomaterial possessed different structural and biological properties. The top layer – Cur/WPI (mimicking the “cartilage layer”) exhibited a lower roughness as compared to the bottom layer – Cur/WPI/HAp (mimicking the “subchondral bone layer”). Cur/WPI was found to exhibit mechanical properties comparable with those of the natural cartilage. While the Young’s modulus of the Cur/WPI/HAp was lower than that of a subchondral bone (and similar to that of Cur/WPI), it was still higher than that of many analogous systems. Cell culture experiments indicated that both biomaterials supported adhesion, spreading, proliferation, and differentiation of ADSCs and BMDSCs *in vitro*, which confirms the very promising biological potential of the fabricated scaffold. The as-observed potential to induce the differentiation of cells without supplementing the media with specific growth factors is most likely connected to high biomimetism (morphological and chemical) of the fabricated scaffolds with the native tissues. Taking into consideration all obtained data, it seems that the novel curdlan-based scaffold is a promising candidate for the osteochondral tissue engineering applications. Nevertheless, for precise determination of the biomedical potential of novel curdlan-based scaffold, the additional *in vitro* experiments (e.g., focused on better quantification of differentiation markers), and also a preclinical *in vivo* study will be performed in future.

Declaration of competing interest

The authors declare that they have no known competing financial interests or personal relationships that could have appeared to influence the work reported in this paper.

Acknowledgments

The authors declare no conflict of interest. The study was partially supported by the Ministry of Science and Higher Education in Poland within the DS2 and DS341 project of Medical University of Lublin, Poland, and by the Ministry of Health of the Czech Republic (grant No.

NU20-08-00208). FTIR analysis carried out by Aleksandra Benko was supported by the National Centre for Research and Development under grant no. LIDER/7/0020/L-11/19/NCBR/2020.The authors would like to thank Krzysztof Skrzypiec from Analytical Laboratory, Maria-Curie Skłodowska University, Lublin, Poland for the help with optical profilometry analysis.

The authors also acknowledge the Light Microscopy Core Facility, IMG ASCR, Prague, Czech Republic, supported by MEYS (LM2018129, CZ.02.1.01/0.0/0.0/18_046/0016045) and RVO – 68378050-KAV-NPUI, for their support with the confocal imaging presented in this manuscript.

Authors Contributions

Katarzyna Klimek: Conceptualization, Methodology, Software, Data curation, Writing – Original draft preparation, Visualization, Investigation, Writing – Reviewing and Editing; **Aleksandra Benko**: Investigation, Methodology, Resources, Software, Data curation, Writing – Original draft preparation, Writing – Reviewing and Editing; **Marta Vandrovcova**: Investigation, Methodology, Writing – Original draft preparation; **Martina Travnickova**: Investigation, Writing – Original draft preparation, Writing – Reviewing and Editing; **Timothy E.L. Douglas**: Investigation, Methodology, Supervision, Writing – Reviewing and Editing; **Marta Tarczynska**: Investigation, Supervision; **Antonin Broz**: Investigation; **Krzysztof Gaweda:** Resources, Supervision, **Grazyna Ginalska**: Project administration, Resources, Supervision, **Lucie Bacakova**: Project administration, Resources, Supervision, Writing – Reviewing and Editing.

References

[1] C. Deng, J. Chang, C. Wu, Bioactive scaffolds for osteochondral regeneration, J. Orthop. Transl. 17 (2019) 15–25. https://doi.org/10.1016/j.jot.2018.11.006.

[2] E. Kon, G. Filardo, F. Perdisa, G. Venieri, M. Marcacci, Clinical results of multilayered biomaterials for osteochondral regeneration, J. Exp. Orthop. 1 (2014) 1–8. https://doi.org/10.1186/s40634-014-0010-0.

[3] Y. Na, Y. Shi, W. Liu, Y. Jia, L. Kong, T. Zhang, C. Han, Y. Ren, Is implantation of autologous chondrocytes superior to microfracture for articular-cartilage defects of the knee? A systematic review of 5-year follow-up data, Int. J. Surg. 68 (2019) 56–62. https://doi.org/10.1016/j.ijsu.2019.06.007.

[4] E. Kon, G. Filardo, A. Di Martino, M. Marcacci, ACI and MACI., J. Knee Surg. 25 (2012) 17–22. https://doi.org/10.1055/s-0031-1299651.

[5] H. Mistry, M. Connock, J. Pink, D. Shyangdan, C. Clar, P. Royle, R. Court, L.C. Biant, A. Metcalfe, N. Waugh, Autologous chondrocyte implantation in the knee: Systematic review and economic evaluation, Health Technol. Assess. (Rockv). 21 (2017) V-160. https://doi.org/10.3310/hta21060.

[6] H. Kwon, W.E. Brown, C.A. Lee, D. Wang, N. Paschos, J.C. Hu, K.A. Athanasiou, Surgical and tissue engineering strategies for articular cartilage and meniscus repair, Nat. Rev. Rheumatol. 15 (2019) 550–570. https://doi.org/10.1038/s41584-019-0255-1.

[7] E. Solheim, J. Hegna, T. Strand, T. Harlem, E. Inderhaug, Randomized Study of Long-term (15-17 Years) Outcome After Microfracture Versus Mosaicplasty in Knee Articular Cartilage Defects, Am. J. Sports Med. 46 (2018) 826–831. https://doi.org/10.1177/0363546517745281.

[8] T.S. Lynch, R.M. Patel, A. Benedick, N.H. Amin, M.H. Jones, A. Miniaci, Systematic review of autogenous osteochondral transplant outcomes, Arthrosc. - J. Arthrosc. Relat. Surg. 31 (2015) 746–754. https://doi.org/10.1016/j.arthro.2014.11.018.

[9] S.J. Seo, C. Mahapatra, R.K. Singh, J.C. Knowles, H.W. Kim, Strategies for osteochondral repair: Focus on scaffolds, J. Tissue Eng. 5 (2014). https://doi.org/10.1177/2041731414541850.

[10] C. Deng, C. Xu, Q. Zhou, Y. Cheng, Advances of nanotechnology in osteochondral regeneration, Wiley Interdiscip. Rev. Nanomedicine Nanobiotechnology. 11 (2019) 1–17. https://doi.org/10.1002/wnan.1576.

[11] P. Nooeaid, V. Salih, J.P. Beier, A.R. Boccaccini, Osteochondral tissue engineering: Scaffolds, stem cells and applications, J. Cell. Mol. Med. 16 (2012) 2247–2270. https://doi.org/10.1111/j.1582-4934.2012.01571.x.

[12] J. Chen, H. Chen, P. Li, H. Diao, S. Zhu, L. Dong, R. Wang, T. Guo, J. Zhao, J. Zhang, Simultaneous regeneration of articular cartilage and subchondral bone in vivo using MSCs induced by a spatially controlled gene delivery system in bilayered integrated scaffolds, Biomaterials. 32 (2011) 4793–4805. https://doi.org/10.1016/j.biomaterials.2011.03.041.

[13] I. Martin, S. Miot, A. Barbero, M. Jakob, D. Wendt, Osteochondral tissue engineering, J. Biomech. 40 (2007) 750–765. https://doi.org/10.1016/j.jbiomech.2006.03.008.

[14] X. Liang, P. Duan, J. Gao, R. Guo, Z. Qu, X. Li, Y. He, H. Yao, J. Ding, Bilayered PLGA/PLGA-HAp Composite Scaffold for Osteochondral Tissue Engineering and Tissue Regeneration, ACS Biomater. Sci. Eng. 4 (2018) 3506–3521.

https://doi.org/10.1021/acsbiomaterials.8b00552.

[15] B. Zhang, J. Huang, R.J. Narayan, Gradient scaffolds for osteochondral tissue engineering and regeneration, J. Mater. Chem. B. 8 (2020) 8149–8170. https://doi.org/10.1039/d0tb00688b.

[16] X. Li, J. Ding, J. Wang, X. Zhuang, X. Chen, Biomimetic biphasic scaffolds for osteochondral defect repair, Regen. Biomater. 2 (2015) 221–228. https://doi.org/10.1093/rb/rbv015.

[17] N.H. Dormer, M. Singh, L. Wang, C.J. Berkland, M.S. Detamore, Osteochondral interface tissue engineering using macroscopic gradients of bioactive signals, Ann. Biomed. Eng. 38 (2010) 2167–2182. https://doi.org/10.1007/s10439-010-0028-0.

[18] C. Parisi, L. Salvatore, L. Veschini, M.P. Serra, C. Hobbs, M. Madaghiele, A. Sannino, L. Di Silvio, Biomimetic gradient scaffold of collagen–hydroxyapatite for osteochondral regeneration, J. Tissue Eng. 11 (2020). https://doi.org/10.1177/2041731419896068.

[19] F. Gao, Z. Xu, Q. Liang, B. Liu, H. Li, Y. Wu, Y. Zhang, Z. Lin, M. Wu, C. Ruan, W. Liu, Direct 3D Printing of High Strength Biohybrid Gradient Hydrogel Scaffolds for Efficient Repair of Osteochondral Defect, Adv. Funct. Mater. 28 (2018) 1–13. https://doi.org/10.1002/adfm.201706644.

[20] P. Lee, O.S. Manoukian, G. Zhou, Y. Wang, W. Chang, X. Yu, S.G. Kumbar, Osteochondral scaffold combined with aligned nanofibrous scaffolds for cartilage regeneration, RSC Adv. 6 (2016) 72246–72255. https://doi.org/10.1039/c6ra08449d.

[21] H. Cai, Y. Yao, Y. Xu, Q. Wang, W. Zou, J. Liang, Y. Sun, C. Zhou, Y. Fan, X. Zhang, A Col I and BCP ceramic bi-layer scaffold implant promotes regeneration in osteochondral defects, RSC Adv. 9 (2019) 3740–3748. https://doi.org/10.1039/c8ra09171d.

[22] V. Condello, G. Filardo, V. Madonna, L. Andriolo, D. Screpis, M. Bonomo, M. Zappia, L.D. Giudici, C. Zorzi, Use of a biomimetic scaffold for the treatment of osteochondral lesions in early osteoarthritis, Biomed Res. Int. 2018 (2018). https://doi.org/10.1155/2018/7937089.

[23] R. Zhang, K.J. Edgar, Properties, chemistry, and applications of the bioactive polysaccharide curdlan, Biomacromolecules. 15 (2014) 1079–1096. https://doi.org/10.1021/bm500038g.

[24] K. Klimek, A. Benko, K. Pałka, A. Ludwiczuk, G. Ginalska, Ion-exchanging dialysis as an effective method for protein entrapment in curdlan hydrogel, Mater. Sci. Eng. C. 105 (2019) 110025. https://doi.org/10.1016/j.msec.2019.110025.

[25] K. Klimek, A. Przekora, K. Pałka, G. Ginalska, New method for the fabrication of highly osteoconductive β-1,3-glucan/HA scaffold for bone tissue engineering: Structural, mechanical, and biological characterization, J. Biomed. Mater. Res. - Part A. 104A (2016) 2528–2536. https://doi.org/10.1002/jbm.a.35798.

[26] K. Klimek, A. Przekora, A. Benko, W. Niemiec, M. Blazewicz, G. Ginalska, The use of calcium ions instead of heat treatment for β-1,3-glucan gelation improves biocompatibility of the β-1,3-glucan/HA bone scaffold, Carbohydr. Polym. 164 (2017)

170–178. https://doi.org/10.1016/j.carbpol.2017.02.015.

[27] A. Belcarz, G. Ginalska, T. Pycka, A. Zima, A. Ślósarczyk, I. Polkowska, Z. Paszkiewicz, W. Piekarczyk, Application of β-1,3-glucan in production of ceramics-based elastic composite for bone repair, Cent. Eur. J. Biol. 8 (2013) 534–548. https://doi.org/10.2478/s11535-013-0169-2.

[28] A. Przekora, G. Ginalska, Addition of 1,3-β-d-glucan to chitosan-based composites enhances osteoblast adhesion, growth, and proliferation, Int. J. Biol. Macromol. 70 (2014) 474–481. https://doi.org/10.1016/j.ijbiomac.2014.07.035.

[29] L. Borkowski, M. Pawłowska, R.P. Radzki, M. Bieńko, I. Polkowska, A. Belcarz, M. Karpiński, T. Słowik, L. Matuszewski, A.˥ósarczyk, G. Ginalska, Effect of a carbonated HAP/β-glucan composite bone substitute on healing of drilled bone voids in the proximal tibial metaphysis of rabbits, Mater. Sci. Eng. C. 53 (2015) 60–67. https://doi.org/10.1016/j.msec.2015.04.009.

[30] D. Gupta, M. Kocot, A.M. Tryba, A. Serafim, I.C. Stancu, Z. Jaegermann, E. Pamuła, G.C. Reilly, T.E.L. Douglas, Novel naturally derived whey protein isolate and aragonite biocomposite hydrogels have potential for bone regeneration, Mater. Des. 188 (2020). https://doi.org/10.1016/j.matdes.2019.108408.

[31] M. Dziadek, K. Charuza, R. Kudlackova, J. Aveyard, R. D’Sa, A. Serafim, I.C. Stancu, H. Iovu, J.G. Kerns, S. Allinson, K. Dziadek, P. Szatkowski, K. Cholewa-Kowalska, L. Bacakova, E. Pamula, T.E.L. Douglas, Modification of heat-induced whey protein isolate hydrogel with highly bioactive glass particles results in promising biomaterial for bone tissue engineering, Mater. Des. 205 (2021) 109749. https://doi.org/10.1016/j.matdes.2021.109749.

[32] M. Dziadek, R. Kudlackova, A. Zima, A. Slosarczyk, M. Ziabka, P. Jelen, S. Shkarina, A. Cecilia, M. Zuber, T. Baumbach, M.A. Surmeneva, R.A. Surmenev, L. Bacakova, K. Cholewa-Kowalska, T.E.L. Douglas, Novel multicomponent organic–inorganic WPI/gelatin/CaP hydrogel composites for bone tissue engineering, J. Biomed. Mater. Res. - Part A. 107 (2019) 2479–2491. https://doi.org/10.1002/jbm.a.36754.

[33] J. Xiang, F. Liu, B. Wang, L. CHen, W. Liu, S. Tan, A Literature Review on Maillard Reaction Based on Milk Products : Advantages , Disadvantages , and Avoidance Strategies, Foods. 10 (2021) 1998. https://doi.org/https://doi.org/10.3390/foods10091998.

[34] K. Klimek, G. Ginalska, Proteins and Peptides as Important Modifiers of the Polymer Scaffolds for Tissue Engineering, Polymers (Basel). 12 (2020) 1–38.

[35] M. Dziadek, T.E.L. Douglas, K. Dziadek, B. Zagrajczuk, A. Serafim, I.C. Stancu, K. Cholewa-Kowalska, Novel whey protein isolate-based highly porous scaffolds modified with therapeutic ion-releasing bioactive glasses, Mater. Lett. 261 (2020) 127115. https://doi.org/10.1016/j.matlet.2019.127115.

[36] S. Wilk, A. Benko, Advances in Fabricating the Electrospun Biopolymer-Based Biomaterials, J. Funct. Biomater. 12 (2021). https://doi.org/https://doi.org/10.3390/jfb12020026.

[37] T.M. O’Shea, X. Miao, Bilayered scaffolds for osteochondral tissue engineering,

Tissue Eng. - Part B Rev. 14 (2008) 447–464. https://doi.org/10.1089/ten.teb.2008.0327.

[38] A. Przekora, K. Klimek, M. Wojcik, K. Palka, G. Ginalska, New method for HA/glucan bone scaffold preparation reduces cytotoxic effect of highly reactive bioceramics, Mater. Lett. 190 (2017). https://doi.org/10.1016/j.matlet.2017.01.033.

[39] A. Przekora, M. Vandrovcova, M. Travnickova, J. Pajorova, M. Molitor, G. Ginalska, L. Bacakova, Evaluation of the potential of chitosan/β-1,3-glucan/hydroxyapatite material as a scaffold for living bone graft production in vitro by comparison of ADSC and BMDSC behaviour on its surface, Biomed. Mater. 12 (2017) 015030. https://doi.org/10.1088/1748-605X/aa56f9.

[40] M. Wojcik, P. Kazimierczak, A. Benko, K. Palka, V. Vivcharenko, A. Przekora, Superabsorbent curdlan-based foam dressings with typical hydrocolloinds properties for highly exuding wound management, Mater. Sci. Eng. C. 124 (2021) 112068. https://doi.org/https://doi.org/10.1016/j.msec.2021.112068.

[41] A. Nurzynska, K. Klimek, K. Palka, Ł. Szajnecki, G. Ginalska, Curdlan-based hydrogels for potential application as dressings for promotion of skin wound healing-preliminary in vitro studies, Materials (Basel). 14 (2021). https://doi.org/10.3390/ma14092344.

[42] A. Nurzynska, K. Klimek, I. Swierzycka, K. Palka, G. Ginalska, Porous Curdlan-Based Hydrogels Modified with Copper Ions as Potential Dressings for Prevention and Management of Bacterial Wound Infection—An In Vitro Assessment, Polymers (Basel). 12 (2020) 1893. https://doi.org/10.3390/polym12091893.

[43] K. Klimek, M. Tarczynska, W. Truszkiewicz, K. Gaweda, T.E.L. Douglas, G. Ginalska, Freeze-Dried Curdlan/Whey Protein Isolate-Based Biomaterial as Promising Scaffold for Matrix-Associated Autologous Chondrocyte Transplantation — A Pilot In-Vitro Study, Cells. 11 (2022) 282. https://doi.org/https://doi.org/10.3390 /cells11020282.

[44] E.S. Gadelmawla, M.M. Koura, T.M.A. Maksoud, I.M. Elewa, H.H. Soliman, Roughness parameters, J. Mater. Process. Technol. 123 (2002) 133–145. https://doi.org/10.1016/S0924-0136(02)00060-2.

[45] M. Travnickova, J. Pajorova, J. Zarubova, N. Krocilova, M. Molitor, L. Bacakova, The Influence of Negative Pressure and of the Harvesting Site on the Characteristics of Human Adipose Tissue-Derived Stromal Cells from Lipoaspirates, Stem Cells Int. 2020 (2020). https://doi.org/10.1155/2020/1016231.

[46] M. Travničková, L. Bačáková, Application of adult mesenchymal stem cells in bone and vascular tissue engineering, Physiol. Res. 67 (2018) 831–850. https://doi.org/10.33549/physiolres.933820.

[47] L. Bacakova, J. Zarubova, M. Travnickova, J. Musilkova, J. Pajorova, P. Slepicka, N.S. Kasalkova, V. Svorcik, Z. Kolska, H. Motarjemi, M. Molitor, Stem cells: their source, potency and use in regenerative therapies with focus on adipose-derived stem cells – a review, Biotechnol. Adv. 36 (2018) 1111–1126. https://doi.org/10.1016/j.biotechadv.2018.03.011.

[48] S.N. Baviskar, A quick & automated method for measuring cell area using ImageJ, Am. Biol. Teach. 73 (2011) 554–556. https://doi.org/10.1525/abt.2011.73.9.9.

[49] K.Q. Liu, Y.N. Liu, Z.G. Duan, X.X. Ma, D. Di Fan, A biomimetic bi-layered tissue engineering scaffolds for osteochondral defects repair, Sci. China Technol. Sci. (2020). https://doi.org/10.1007/s11431-020-1597-4.

[50] L. Fu, Z. Yang, C. Gao, H. Li, Z. Yuan, F. Wang, X. Sui, S. Liu, Q. Guo, Advances and prospects in biomimetic multilayered scaffolds for articular cartilage regeneration, Regen. Biomater. 7 (2020) 527–542. https://doi.org/10.1093/RB/RBAA042.

[51] A.B. Faia-Torres, S. Guimond-Lischer, M. Rottmar, M. Charnley, T. Goren, K. Maniura-Weber, N.D. Spencer, R.L. Reis, M. Textor, N.M. Neves, Differential regulation of osteogenic differentiation of stem cells on surface roughness gradients, Biomaterials. 35 (2014) 9023–9032. https://doi.org/10.1016/j.biomaterials.2014.07.015.

[52] A.B. Faia-Torres, M. Charnley, T. Goren, S. Guimond-Lischer, M. Rottmar, K. Maniura-Weber, N.D. Spencer, R.L. Reis, M. Textor, N.M. Neves, Osteogenic differentiation of human mesenchymal stem cells in the absence of osteogenic supplements: A surface-roughness gradient study, Acta Biomater. 28 (2015) 64–75. https://doi.org/10.1016/j.actbio.2015.09.028.

[53] X. Cun, L. Hosta-Rigau, Topography: A biophysical approach to direct the fate of mesenchymal stem cells in tissue engineering applications, Nanomaterials. 10 (2020) 1–41. https://doi.org/10.3390/nano10102070.

[54] Y. Hou, W. Xie, L. Yu, L.C. Camacho, C. Nie, M. Zhang, R. Haag, Q. Wei, Surface Roughness Gradients Reveal Topography-Specific Mechanosensitive Responses in Human Mesenchymal Stem Cells, Small. 16 (2020) 1–10. https://doi.org/10.1002/smll.201905422.

[55] L. Xinya, R.A. Weiss, Relationship between the Glass Transition Temperature and the Interaction Parameter of Miscible Binary Polymer Blends, Macromolecules. 25 (1992) 3242–3246. https://doi.org/10.1021/ma00038a033.

[56] S. Pastoriza, J. Quesada, J.A. Rufián-Henares, Lactose and Oligosaccharides: Maillard Reaction ☆, in: Ref. Modul. Food Sci., 2018: pp. 1–19. https://doi.org/10.1016/b978-0-08-100596-5.22552-3.

[57] W.Q. Wang, Y.H. Bao, Y. Chen, Characteristics and antioxidant activity of water-soluble Maillard reaction products from interactions in a whey protein isolate and sugars system, Food Chem. 139 (2013) 355–361. https://doi.org/10.1016/j.foodchem.2013.01.072.

[58] Q. Liu, J. Li, B. Kong, P. Li, X. Xia, Physicochemical and antioxidant properties of Maillard reaction products formed by heating whey protein isolate and reducing sugars, Int. J. Dairy Technol. 67 (2014) 220–228. https://doi.org/10.1111/1471-0307.12110.

[59] M. Karbasi, G. Askari, Modification of whey protein microgel particles with mono-oligo- and polysaccharides through the Maillard reaction: Effects on structural and techno-functional properties, Food Struct. 28 (2021) 100184. https://doi.org/10.1016/j.foostr.2021.100184.

[60] A. Ioannou, V. Daskalakis, C. Varotsis, Detection of Maillard reaction products by a coupled HPLC-Fraction collector technique and FTIR characterization of Cu(II)-complexation with the isolated species, J. Mol. Struct. 1141 (2017) 634–642. https://doi.org/10.1016/j.molstruc.2017.04.011.

[61] K. Klimek, A. Benko, K. Pałka, A. Ludwiczuk, G. Ginalska, Ion-exchanging dialysis as an effective method for protein entrapment in curdlan hydrogel, Mater. Sci. Eng. C. 105 (2019). https://doi.org/10.1016/j.msec.2019.110025.

[62] A. Przekora, A. Benko, M. Blazewicz, G. Ginalska, Hybrid chitosan/β-1,3-glucan matrix of bone scaffold enhances osteoblast adhesion, spreading and proliferation via promotion of serum protein adsorption, Biomed. Mater. 11 (2016) 45001. https://doi.org/10.1088/1748-6041/11/4/045001.

[63] E. Gómez-Ordóñez, P. Rupérez, FTIR-ATR spectroscopy as a tool for polysaccharide identification in edible brown and red seaweeds, Food Hydrocoll. 25 (2011) 1514–1520. https://doi.org/10.1016/j.foodhyd.2011.02.009.

[64] P. Garidel, H. Schott, Fourier-Transform Midinfrared Spectroscopy for Analysis and Screening of Liquid Protein Forumations, Part 1, Bioprocess Int. 18 (2006) 2299–2314.

[65] A. Barth, Infrared spectroscopy of proteins, Biochim. Biophys. Acta - Bioenerg. 1767 (2007) 1073–1101. https://doi.org/10.1016/j.bbabio.2007.06.004.

[66] B. Behera, P.K. Das, Blue- and Red-Shifting Hydrogen Bonding: A Gas Phase FTIR and Ab Initio Study of RR′CO···DCCl3 and RR′S···DCCl3 Complexes, J. Phys. Chem. A. 122 (2018) 4481–4489. https://doi.org/10.1021/acs.jpca.7b11962.

[67] Y.H. Cheng, D.C. Mu, Y. Jiao, Z. Xu, M.L. Chen, Microwave-assisted maillard reaction between rice protein and dextran induces structural changes and functional improvements, J. Cereal Sci. 97 (2021) 103134. https://doi.org/10.1016/j.jcs.2020.103134.

[68] V.A. Sinyayev, gulparshyn A. Toxeitova, A.A. Batyrbayeva, L.R. Sassykova, R.N. Azhigulova, Y.N. Sakhipov, A comparative investigtion of the IR spectra of a carbohydrate series, J. Chem. Technol. Metall. 55 (2020) 724–729.

[69] K. Wang, W. Li, K. Wang, Z. Hu, H. Xiao, B. Du, L. Zhao, Structural and inflammatory characteristics of Maillard reaction products from litchi thaumatin-like protein and fructose, Food Chem. 374 (n.d.) 131821. https://doi.org/https://doi.org/10.1016/j.foodchem.2021.131821.

[70] F.L. Gu, J.M. Kim, S. Abbas, X.M. Zhang, S.Q. Xia, Z.X. Chen, Structure and antioxidant activity of high molecular weight Maillard reaction products from casein-glucose, Food Chem. 120 (2010) 505–511. https://doi.org/10.1016/j.foodchem.2009.10.044.

[71] B. Ye, J. Chen, H. Ye, Y. Zhang, Q. Yang, H. Yu, L. Fu, Y. Wang, Development of a time-temperature indicator based on Maillard reaction for visually monitoring the freshness of mackerel, Food Chem. 373 (2022) 131448. https://doi.org/https://doi.org/10.1016/j.foodchem.2021.131448.

[72] Q. Xiao, M.W. Woo, J. Hu, H. Xiong, Q. Zhao, The role of heating time on the characteristics, functional properties and antioxidant activity of enzyme-hydrolyzed

rice proteins-glucose Maillard reaction products, Food Biosci. 43 (2021) 101225. https://doi.org/10.1016/j.fbio.2021.101225.

[73] Y. Yang, S.W. Cui, J. Gong, Q. Guo, Q. Wang, Y. Hua, A soy protein-polysaccharides Maillard reaction product enhanced the physical stability of oil-in-water emulsions containing citral, Food Hydrocoll. 48 (2015) 155–164. https://doi.org/10.1016/j.foodhyd.2015.02.004.

[74] B. Nayak, P.K. Misra, Recognition of the surface characteristics and electrical properties of a nanocrystalline hydroxyapatite synthesized from Pila globosa shells for versatile applications, Mater. Chem. Phys. 230 (2019) 187–196. https://doi.org/10.1016/j.matchemphys.2019.03.068.

[75] P. Kazimierczak, A. Benko, K. Palka, C. Canal, D. Kolodynska, A. Przekora, Novel synthesis method combining a foaming agent with freeze-drying to obtain hybrid highly macroporous bone scaffolds, J. Mater. Sci. Technol. 43 (2020) 52–63. https://doi.org/10.1016/j.jmst.2020.01.006.

[76] N. Sachot, E. Engel, O. Castano, Hybrid Organic-Inorganic Scaffolding Biomaterials for Regenerative Therapies, Curr. Org. Chem. 18 (2014) 2299–2314. https://doi.org/10.2174/1385272819666140806200355.

[77] K. Gkioni, S.C.G. Leeuwenburgh, T.E.L. Douglas, A.G. Mikos, J.A. Jansen, Mineralization of hydrogels for bone regeneration, Tissue Eng. - Part B Rev. 16 (2010) 577–585. https://doi.org/10.1089/ten.teb.2010.0462.

[78] A.E. Peters, R. Akhtar, E.J. Comerford, K.T. Bates, The effect of ageing and osteoarthritis on the mechanical properties of cartilage and bone in the human knee joint, Sci. Rep. 8 (2018) 1–13. https://doi.org/10.1038/s41598-018-24258-6.

[79] H. Xiao, W. Huang, K. Xiong, S. Ruan, C. Yuan, G. Mo, R. Tian, S. Zhou, R. She, P. Ye, B. Liu, J. Deng, Osteochondral repair using scaffolds with gradient pore sizes constructed with silk fibroin, chitosan, and nano-hydroxyapatite, Int. J. Nanomedicine. 14 (2019) 2011–2027. https://doi.org/10.2147/IJN.S191627.

[80] K. Klimek, A. Belcarz, R. Pazik, P. Sobierajska, T. Han, R.J. Wiglusz, G. Ginalska, “False” cytotoxicity of ions-adsorbing hydroxyapatite - Corrected method of cytotoxicity evaluation for ceramics of high specific surface area, Mater. Sci. Eng. C. 65 (2016) 70–79. https://doi.org/10.1016/j.msec.2016.03.105.

[81] P.B. Malafaya, R.L. Reis, Bilayered chitosan-based scaffolds for osteochondral tissue engineering: Influence of hydroxyapatite on in vitro cytotoxicity and dynamic bioactivity studies in a specific double-chamber bioreactor, Acta Biomater. 5 (2009) 644–660. https://doi.org/10.1016/j.actbio.2008.09.017.

[82] P. Wang, L. Zhao, W. Chen, X. Liu, M.D. Weir, H.H.K. Xu, Stem cells and calcium phosphate cement scaffolds for bone regeneration, J. Dent. Res. 93 (2014) 618–625. https://doi.org/10.1177/0022034514534689.

[83] C. Gao, S. Peng, P. Feng, C. Shuai, Bone biomaterials and interactions with stem cells, Bone Res. 5 (2017) 1–33. https://doi.org/10.1038/boneres.2017.59.

[84] E. Bosch-Rué, L. Diez-Tercero, B. Giordano-Kelhoffer, L.M. Delgado, B.M. Bosch, M. Hoyos-Nogués, M.A. Mateos-Timoneda, P.A. Tran, F.J. Gil, R.A. Perez, Biological

Roles and Delivery Strategies for Ions to Promote Osteogenic Induction, Front. Cell Dev. Biol. 8 (2021). https://doi.org/10.3389/fcell.2020.614545.

[85] L.F. Mellor, M. Mohiti-Asli, J. Williams, A. Kannan, M.R. Dent, F. Guilak, E.G. Loboa, Extracellular Calcium Modulates Chondrogenic and Osteogenic Differentiation of Human Adipose-Derived Stem Cells: A Novel Approach for Osteochondral Tissue Engineering Using a Single Stem Cell Source, Tissue Eng. - Part A. 21 (2015) 2323–2333. https://doi.org/10.1089/ten.tea.2014.0572.

[86] M.N. Lee, H.S. Hwang, S.H. Oh, A. Roshanzadeh, J.W. Kim, J.H. Song, E.S. Kim, J.T. Koh, Elevated extracellular calcium ions promote proliferation and migration of mesenchymal stem cells via increasing osteopontin expression, Exp. Mol. Med. 50 (2018). https://doi.org/10.1038/s12276-018-0170-6.

[87] B. Feng, J. Weng, B.C. Yang, S.X. Qu, X.D. Zhang, Characterization of titanium surfaces with calcium and phosphate and osteoblast adhesion, Biomaterials. 25 (2004) 3421–3428. https://doi.org/10.1016/j.biomaterials.2003.10.044.

[88] S. Gopal, H.A.B. Multhaupt, J.R. Couchman, Calcium in Cell-Extracellular Martix Interactions, Adv. Exp. Med. Biol. 1131 (2020) 1079–1102. https://doi.org/doi: 10.1007/978-3-030-12457-1_43.

[89] S. Mohamed-Ahmed, I. Fristad, S.A. Lie, S. Suliman, K. Mustafa, H. Vindenes, S.B. Idris, Adipose-derived and bone marrow mesenchymal stem cells: A donor-matched comparison, Stem Cell Res. Ther. 9 (2018) 1–15. https://doi.org/10.1186/s13287-018-0914-1.

[90] S. Mohamed-Ahmed, M.A. Yassin, A. Rashad, H. Espedal, S.B. Idris, A. Finne-Wistrand, K. Mustafa, H. Vindenes, I. Fristad, Comparison of bone regenerative capacity of donor-matched human adipose–derived and bone marrow mesenchymal stem cells, Cell Tissue Res. 383 (2021) 1061–1075. https://doi.org/10.1007/s00441-020-03315-5.

[91] S.H. Wu, Y.T. Liao, C.H. Huang, Y.C. Chen, E.R. Chiang, J.P. Wang, Comparison of the confluence-initiated neurogenic differentiation tendency of adipose-derived and bone marrow-derived mesenchymal stem cells, Biomedicines. 9 (2021). https://doi.org/10.3390/biomedicines9111503.

[92] Y. Ikegame, K. Yamashita, S.I. Hayashi, H. Mizuno, M. Tawada, F. You, K. Yamada, Y. Tanaka, Y. Egashira, S. Nakashima, S.I. Yoshimura, T. Iwama, Comparison of mesenchymal stem cells from adipose tissue and bone marrow for ischemic stroke therapy, Cytotherapy. 13 (2011) 675–685. https://doi.org/10.3109/14653249.2010.549122.

[93] S. Chen, J. Zhu, M. Wang, Y. Huang, Z. Qiu, J. Li, X. Chen, H. Chen, M. Xu, J. Liu, M. She, H. Li, X. Yang, Y. Wang, X. Cai, Comparison of the therapeutic effects of adipose-derived and bone marrow mesenchymal stem cells on erectile dysfunction in diabetic rats, Int. J. Mol. Med. 44 (2019) 1006–1014. https://doi.org/10.3892/ijmm.2019.4254.

[94] S. Mohamed-Ahmed, I. Fristad, S.A. Lie, S. Suliman, K. Mustafa, H. Vindenes, S.B. Idris, Adipose-derived and bone marrow mesenchymal stem cells: A donor-matched comparison, Stem Cell Res. Ther. 9 (2018) 1–16. https://doi.org/10.1186/s13287-018-

0914-1.

[95] M.M. Stevens, J.H. George, Exploring and engineering the cell surface interface, Science (80-.). 310 (2005) 1135–1138. https://doi.org/10.1126/science.1106587.

[96] B.P. Chan, K.W. Leong, Scaffolding in tissue engineering: General approaches and tissue-specific considerations, Eur. Spine J. 17 (2008) S467–S479. https://doi.org/10.1007/s00586-008-0745-3.

[97] P. Kazimierczak, A. Benko, M. Nocun, A. Przekora, Novel chitosan / agarose / hydroxyapatite nanocomposite scaffold for bone tissue engineering applications : comprehensive evaluation of biocompatibility and osteoinductivity with the use of osteoblasts and mesenchymal stem cells, Int. J. Nanomedicine. 14 (2019) 6615–6630. https://doi.org/10.2147/IJN.S217245.

[98] F. Olate-Moya, L. Arens, M. Wilhelm, M.A. Mateos-Timoneda, E. Engel, H. Palza, Chondroinductive Alginate-Based Hydrogels Having Graphene Oxide for 3D Printed Scaffold Fabrication, ACS Appl. Mater. Interfaces. 12 (2020) 4343–4357. https://doi.org/10.1021/acsami.9b22062.

[99] S. Abedin Dargoush, S. Irani, A. Naderi Sohi, M. Soleimani, H. Hanaee-Ahvaz, Chondroinductive impact of polyethersulfone/benzyl hyaluronate nanofibrous scaffold on human mesenchymal stem cells, Polym. Adv. Technol. 31 (2020) 2569–2578. https://doi.org/10.1002/pat.4984.

[100] P. Kazimierczak, E. Syta, A. Przekora, G. Ginalska, Comparison of osteogenic differentiation ability between bone marrow-derived mesenchymal stem cells and adipose tissue-derived mesenchymal stem cells, Med. Ogólna i Nauk. o Zdrowiu. 24 (2018) 101–106. https://doi.org/10.26444/monz/92078.

[101] X. Xie, Y. Wang, C. Zhao, S. Guo, S. Liu, W. Jia, R.S. Tuan, C. Zhang, Comparative evaluation of MSCs from bone marrow and adipose tissue seeded in PRP-derived scaffold for cartilage regeneration, Biomaterials. 33 (2012) 7008–7018. https://doi.org/10.1016/j.biomaterials.2012.06.058.

[102] Y. Yang, Q. Zhang, T. Xu, H. Zhang, M. Zhang, L. Lu, Y. Hao, J.Y.H. Fuh, X. Zhao, Photocrosslinkable nanocomposite ink for printing strong, biodegradable and bioactive bone graft, Biomaterials. 263 (2020). https://doi.org/10.1016/j.biomaterials.2020.120378.

[103] Y. Yang, T. Xu, Q. Zhang, Y. Piao, H.P. Bei, X. Zhao, Biomimetic, Stiff, and Adhesive Periosteum with Osteogenic–Angiogenic Coupling Effect for Bone Regeneration, Small. 17 (2021) 1–10. https://doi.org/10.1002/smll.202006598.

[104] R.K. Schneider, A. Puellen, R. Kramann, K. Raupach, J. Bornemann, R. Knuechel, A. Pérez-Bouza, S. Neuss, The osteogenic differentiation of adult bone marrow and perinatal umbilical mesenchymal stem cells and matrix remodelling in three-dimensional collagen scaffolds, Biomaterials. 31 (2010) 467–480. https://doi.org/10.1016/j.biomaterials.2009.09.059.

Figure Captions

Fig. 1. Stereoscopic microscope images showing a biphasic curdlan-based osteochondral scaffold (A) and an example of osteochondral autograft harvested during mosaicplasty procedure (B); magnification 8x, scale bar = 2 mm.

Fig. 2. Scanning electron microscope images showing longitudinal cross-section of a biphasic curdlan-based scaffold (A), the top layer (B) and the bottom layer (C) of this biomaterial; magnification 75x or150x, scale bar = 100 μm.

Fig. 3. The 3D optical profilometry images showing topography of the top layer (A) and the bottom layer (B) of the biphasic curdlan-based scaffold. Based on the obtained images, the following roughness parameters were calculated (Vision64 Map Software; Bruker, USA): arithmetic average height (R_a), maximum height of peaks (R_p), root mean square roughness (R_q), maximum height of the profile (R_t), and maximum depth of valleys (R_v) (C).

Fig 4. The FTIR-ATR spectra of the composites and their compounds: “cartilage layer” (A) and “subchondral bone layer” (B). For better clarity, the spectra are offset and maximized in two separate regions in which characteristic bands are present: from 4000 to 2700 cm^{-1} and from 1800 to 500 cm^{-1}. Stereoscopic microscope images of the compounds and the composite (C); magnification 10x, scale bar = 1 mm.

Fig 5. Some examples of the initial and intermediate stages of the Maillard reaction. The saccharides are presented in the Haworth projection. Only the end, reducing unit of the polysaccharide chain is shown during the reaction, but more units having the aldehyde functional group can be formed in the course of the process through chain and sugar fragmentation. In real life conditions, the reaction is known to yield more than 100 different products [56].

Fig 6. The FTIR-ATR spectra of the “subchondral bone layer” and its biopolymeric compound. The spectra are normalized in the 1715 – 1475 cm^{-1} region and are presented in the two spectral regions: from 4000 to 2700 cm^{-1} and from 1800 to 1120 cm^{-1}.

Fig. 7. Stress-strain curves (A) and Young’s modulus values (B) for the investigated biomaterials: Cur/WPI, Cur/WPI/HAp and biphasic Cur/WPI-Cur/WPI/HAp. The results were obtained using 5 separate biomaterials (n=5). The differences between samples were not statistically significant.

Fig. 8. Swelling ability of the biphasic Cur/WPI-Cur/WPI/HAp biomaterial. It was presented as an increase in its weight (Wi) after soaking in 0.9% NaCl solution.

Fig. 9. Ion-reactivity of Cur/WPI and Cur/WPI/HAp biomaterials. The changes in concentration of Ca^{2+} (A) and HPO_4^{2-} (B) ions in the culture medium were evaluated during 15-day incubation. * Statistically significant differences between concentration of ions in the culture medium after incubation with Cur/WPI and concentration of ions in the culture medium after incubation with Cur/WPI/HAp; $^{\$}$ Statistically significant differences between concentration of ions in the culture medium after incubation with Cur/WPI and concentration of ions in the culture medium before incubation (day 0); $^{\#}$ Statistically significant differences between concentration of ions in the culture medium after incubation with Cur/WPI/HAp and concentration of ions in the culture medium before incubation (day 0), according to an One-Way ANOVA test followed by Tukey’s multiple comparison, $P < 0.05$.

Fig.10. Confocal microscope images demonstrating adhesion of human adipose tissue-derived mesenchymal stem cells (ADSCs) and human bone marrow-derived mesenchymal stem cells (BMDSCs) to the surface of Cur/WPI and Cur/WPI/HAp biomaterials. Nuclei – blue fluorescence, F-actin – red fluorescence. Visible blue fluorescence in the structure of biomaterials was emitted by WPI; objective magnification 10x, scale bar =150 µm.

Fig.11. Quantification of the spreading area of human adipose tissue-derived mesenchymal stem cells (ADSCs) and human bone marrow-derived mesenchymal stem cells (BMDSCs) after 48-hour culture on the surface of Cur/WPI and Cur/WPI/HAp biomaterials. The results were expressed as average value of spreading area [μm^2] per one cell. * Statistically significant differences compared to the Cur/WPI biomaterial, according to One-way ANOVA test followed by Tukey's multiple comparison, $P < 0.05$.

Fig.12. Proliferation of human adipose tissue-derived mesenchymal stem cells (ADSCs) (A) and human bone marrow-derived mesenchymal stem cells (BMDSCs) (B) after 2-, 5-, and 8-day culture on the polystyrene (PS, control) and surface of Cur/WPI and Cur/WPI/HAp biomaterials. The results were obtained using the resazurin assay.* Statistically significant differences compared to control (PS); $^\$$Statistically significant differences between Cur/WPI and Cur/WPI/HAp at specified time of incubation; $^\#$ Statistically significant differences compared to results obtained on day 2; $^\%$ Statistically significant differences compared to results obtained on day 5; according to One-way ANOVA test followed by Tukey's multiple comparison, $P < 0.05$.

Fig. 13. Confocal microscope images demonstrating chondrogenic differentiation of human adipose tissue-derived mesenchymal stem cells (ADSCs) after 15-day culture on the surface of the Cur/WPI and Cur/WPI/HAp biomaterials. The cells were cultured in the chondrogenic medium (+ supplements) or in the growth culture medium (- supplements). Nuclei – blue fluorescence, collagen II; aggrecan; SOX-9 – green fluorescence. Visible blue fluorescence in the structure of biomaterials was emitted by WPI; objective magnification 10x, scale bar =150 μm.

Fig. 14. Confocal microscope images demonstrating chondrogenic differentiation of human bone marrow-derived mesenchymal stem cells (BMDSCs) after 15-day culture on the surface of the Cur/WPI and Cur/WPI/HAp biomaterials. The cells were cultured in the chondrogenic

medium (+ supplements) or in the growth culture medium (- supplements). Nuclei – blue fluorescence, collagen II; aggrecan; SOX-9 – green fluorescence. Visible blue fluorescence in the structure of biomaterials was emitted by WPI; objective magnification 10x, scale bar =150 μm.

Fig. 15. Confocal microscope images demonstrating osteogenic differentiation of human adipose tissue-derived mesenchymal stem cells (ADSCs) after 15-day culture on the surface of the Cur/WPI and Cur/WPI/HAp biomaterials. The cells were cultured in the osteogenic medium (+ supplements) or in the growth culture medium (- supplements). Nuclei – blue fluorescence, collagen I; alkaline phosphatase (ALP); osteocalcin – green fluorescence. Visible blue fluorescence in the structure of biomaterials was emitted by WPI; objective magnification 10x, scale bar =150 μm.

Fig. 16. Confocal microscope images demonstrating osteogenic differentiation of human bone marrow-derived mesenchymal stem cells (BMDSCs) after 15-day culture on the surface of the Cur/WPI and Cur/WPI/HAp biomaterials. The cells were cultured in the osteogenic medium (+ supplements) or in the growth culture medium (- supplements). Nuclei – blue fluorescence, collagen I; alkaline phosphatase (ALP); osteocalcin – green fluorescence. Visible blue fluorescence in the structure of biomaterials was emitted by WPI; objective magnification 10x, scale bar =150 μm.